

Dynamic Active Constraints for Surgical Robots using Vector Field Inequalities

Murilo M. Marinho, *Student Member, IEEE*, Bruno V. Adorno, *Senior Member, IEEE*, Kanako Harada, *Member, IEEE*, and Mamoru Mitsuishi, *Member, IEEE*

Abstract—Robotic assistance allows surgeons to perform dexterous and tremor-free procedures, but robotic aid is still underrepresented in procedures with constrained workspaces, such as deep brain neurosurgery and endonasal surgery. In those, surgeons have restricted vision to areas near the surgical tool tips, which increases the risk of unexpected collisions between the shafts of the instruments and their surroundings, in special when those parts are outside the surgical field-of-view. Dynamic active constraints can be used to prevent collisions between moving instruments and prevent damage to static or moving tissues. In this work, our vector field inequality method is extended to provide dynamic active constraints to any number of robots and moving objects sharing the same workspace. The method is evaluated in experiments and simulations in which the robot tools have to avoid collisions, autonomously and in real-time, with a constrained endonasal surgical environment and between each other. Results show that both manipulator-manipulator and manipulator-boundary collisions can be effectively prevented using the vector field inequalities.

Index Terms—virtual fixtures; collision avoidance; dual quaternions; optimization-based control

I. INTRODUCTION

MICROSURGERY requires surgeons to operate with submillimeter precision while handling long thin tools and viewing the workspace through an endoscope or microscope. For instance, in endonasal and deep neurosurgery, surgeons use a pair of 100-300mm long 3-4mm diameter instruments. Furthermore, whereas in endonasal surgery images are obtained with a 4mm diameter endoscope, deep neurosurgery requires a microscope. The workspace in both cases can be approximated by a 80-110mm long truncated cone with 20-30mm diameter [1], [2].

In hands-on microsurgery, the surgeon is fully aware of the tools' positions with respect to the workspace and is able to feel forces to prevent damage to structures. However, constant collisions between surrounding tissues and other instruments

reduce surgeon dexterity and increases the difficulty of the task. As vision is often limited to a region near the surgical tool tips, it is difficult for the surgeons to compensate for restrictions induced by unseen collision points. Moreover, the disturbance caused by hand tremor may be larger than the structures being treated, which is problematic as accuracy is paramount in those surgical procedures. In this context, robots are used as an assistive equipment to increase accuracy and safety, and to reduce hand tremor and mental load [1]–[6].

To increase accuracy and attenuate hand tremor, most surgical robots are commanded in task space coordinates either through teleoperation [1], [3]–[6] or comanipulation [7], [8]. Motion commands go through a scaling and/or filtering stage, whose output is used to generate joint space control inputs by using a kinematic control law based on the robot differential kinematics [9]. Kinematic control laws are valid when low accelerations are imposed in the joint space, and are ubiquitous in control algorithms designed for surgical robotics [10], [11] since low accelerations are expected in those scenarios. In microsurgery, slow and low amplitude motions are the rule.

Together with such kinematic control laws, active constraints (virtual fixtures) can be used in order to provide an additional layer of safety to keep the surgical tool from entering a restricted region, or from leaving a safe region, even if the robot is commanded otherwise [10], [11]. A thorough survey on active constraints was done by Bowyer *et al.* [12]. More recent papers published after that survey presented the use of guidance virtual fixtures to assist in knot tying in robotic laparoscopy [13], and used virtual fixtures to allow surgeons to feel the projected force feedback from the distal end of a tool to the proximal end of a tool in a comanipulation context [14].

In real applications, some of the objects in the surgical workspace are dynamic. Usually those elements are other tools sharing the same restricted workspace or moving organs. Most of the literature in dynamic active constraints regards the latter and, more specifically, the development of techniques to avoid collisions between tool tip and the beating heart [15]–[18]. For instance, Gibo *et al.* [15] studied the proxy method with moving forbidden zones, Ryden and Chizeck [18] proposed virtual fixtures for dynamic restricted zones using point clouds, and Ren *et al.* [19] proposed dynamic active constraints using medical images to build potential fields, all aiming to reduce contact force between tool tip and the beating heart surface. A work that considered the entire robot instead of just the tool tip was proposed by Kwok *et al.* [20], who developed a control framework for a snake robot based on an optimization

This research was funded by the ImPACT Program of the Council for Science, Technology and Innovation (Cabinet Office, Government of Japan).

Murilo M. Marinho, Kanako Harada, and Mamoru Mitsuishi are with the Department of Mechanical Engineering, the University of Tokyo, Tokyo, Japan. Email: {murilo, kanako, mamoru}@nml.t.u-tokyo.ac.jp. Murilo M. Marinho has been supported by the Japanese Ministry of Education, Culture, Sports, Science, and Technology (MEXT).

Bruno V. Adorno is with the Department of Electrical Engineering and with the Graduate Program in Electrical Engineering - Federal University of Minas Gerais, Belo Horizonte-MG, Brazil. Email: adorno@ufmg.br. Bruno V. Adorno has been supported by the Brazilian agencies CAPES, CNPq, FAPEMIG, and by the project INCT (National Institute of Science and Technology) under the grant CNPq (Brazilian National Research Council) 465755/2014-3, FAPESP (São Paulo Research Foundation) 2014/50851-0.

problem. That work used dynamic active constraints in the context of beating heart surgery [16] and guidance virtual fixtures [21], both of which were specialized for snake-robots.

A. Enforcement of constraints

Literature on static and moving virtual fixtures is generally focused on interactions between the tool tip and the environment. In those cases, generating force feedback in the master side is quite straightforward and may be enough to avoid damaging healthy tissue. In microsurgery, however, interactions also occur far from the tool tips. Indeed, our long-standing cooperation with medical doctors [1], [2], [4]–[6] indicates that, as the workspace is highly constrained, surgical tools may suffer collisions along their structures, whose effects in the tool tip can be complex; therefore, effectively projecting those collisions to the master interface for effective force feedback is challenging.

Other forms of feedback, such as visual cues [6], [22], that warn the user about proximity to restricted regions can be ineffective when using redundant robotic systems [1], since the mapping between the master interface and the robot configuration is not one to one. In such cases, moving the tool tip in a given direction may correspond to an infinite number of configurations due to redundancy, which can be counterintuitive for the surgeon as the same tool tip trajectory can correspond to collision-free motions or motions with collision, depending on the robot configuration. In fact, it is safer and simpler if the robot avoids restricted zones—in special those outside the field-of-view—autonomously. This way, the increasing prevalence of redundant robots is turned into an advantage, if used together with a proper control framework as the one proposed in this work.

B. Related work

To the best of the authors’ knowledge, the framework in the medical robotics literature that more closely meets microsurgical requirements is the one initially developed by Funda *et al.* [23], which uses quadratic programming. That framework does not require a specific robot geometry, it can handle points in the robot besides the tool tip, and also considers equality and inequality constraints, which gives hard distance limits between any point in the manipulator and objects in the environment. That framework was extended by Kapoor *et al.* [10], who developed a library of virtual fixtures using five task primitives that can be combined into customized active constraints using nonlinear constraints or linear *approximations*. Li *et al.* [11] used the extended framework to aid the operators in moving, without collision, a single surgical tool in a highly constrained space in sinus surgery; however, due to how the obstacles were modeled using a covariance tree, which requires a long computational time, dynamic virtual fixtures cannot be considered [19], [20].

In prior approaches [10], [11], [15]–[18], [20], [21], [23], obstacle constraints are activated whenever the robot reaches the boundary of a restricted zone, which might result in acceleration peaks. Some authors attempted to address this issue. For instance, Xia *et al.* [24] reduced the proportional

gain in an admittance control law proportionally to the distance between the tool tip and the nearest obstacle. This allowed the system to smoothly avoid collisions, but also impeded motion tangential to the obstacle boundary. Prada and Payandeh [25] proposed adding a time-varying gain to smooth the attraction force of attractive virtual fixtures.

Outside of active constraints/virtual fixtures literature, Faverjon and Tournassoud [26] proposed a path planner based on velocity dampers, which are an alternative to potential fields, to allow the generation of restricted zones without affecting tangential motion. His technique was evaluated in simulations of a manipulator navigating through a nuclear reactor. To reduce computational costs, his method used the *approximate* distance between convex solids obtained through iterative optimization. Kanoun *et al.* [27] extended velocity dampers to a task-priority framework. Their technique was validated in a simulated humanoid robot.

Finding the exact distance and distance derivative between different relevant primitives can increase computational speed and accuracy. This is of high importance in microsurgical applications, as properly using the constrained workspace might require the tool shafts to get arbitrarily close to each other without collision, in addition to the fact that all calculations must be performed in real-time.

C. Statement of contributions

In our prior work¹ [28], the concept of vector field inequalities applied for active constraints was first introduced. Primitives were found involving the distance between static elements and one dynamic element kinematically coupled to the robot. A proof-of-concept study was done in a simulation of deep neurosurgery, in which a pair of robots shared the same constrained workspace and *only one* of the robots moved. Therefore, the static robot was considered as an obstacle for the moving one.

In this work, we further extend the research done in [28]. First, we extend the framework to take into consideration dynamic active constraints, which may include any number of robotic systems sharing the same workspace as well as dynamic objects whose velocity can be tracked or estimated. The distance and its derivative between elements is found algebraically, allowing accurate and fast computation of the constraints, which is paramount for real-time evaluation in microsurgical settings. In addition, we introduce more relevant primitives that are coupled to the robots in order to enrich the description of constraints. Second, we evaluate the dynamic active constraints framework in in-depth simulation studies, which demonstrate the advantages of dynamic active constraints over static ones. Third, the framework is implemented in a physical system composed of a pair of robotic manipulators. Experiments are performed, including an autonomous tool tip tracing experiment using a realistic endonasal surgical setup, with an anatomically correct 3D printed head model, in which active constraints are used to avoid collisions.

In contrast with prior techniques in the medical robotics literature [10], [11], [15]–[18], [20], [21], [23], our technique

¹Preprint available at <https://arxiv.org/abs/1804.03883>.

provides smooth velocities at the boundary of restricted zones. Moreover, it does not disturb or prevent tangential velocities, differently from [24] and [25]. When considering specifically the literature on dynamic active constraints, our technique considers an arbitrary number of simultaneous frames in the robot, not only the tool tip as in [15]–[18]; furthermore, it is applicable to general robot geometry, in contrast to solutions for snake robots [16], [20], [21]. Outside of the medical robotics applications, our framework is a generalization of velocity dampers [26].

D. Organization of the paper

Section II introduces the required mathematical background; more specifically, it presents a review of dual quaternion algebra, differential kinematics, and quadratic programming. Section III explains the proposed vector field inequalities and Section IV introduces primitives used to model the relation between points, lines, planes, and to enforce the task's geometrical constraints. Section V presents simulations to evaluate different combinations of dynamic and static active constraints, in addition to experiments in a real platform to evaluate the exponential behavior of the velocity constraint towards a static plane, as well as an experiment in a realistic environment for endonasal surgery. Finally, Section VI concludes the paper and presents suggestions for future works.

II. MATHEMATICAL BACKGROUND

TABLE I
MATHEMATICAL NOTATION.

Notation	Meaning
\mathbb{H}, \mathbb{H}_p	Set of quaternions and pure quaternions (the latter is isomorphic to \mathbb{R}^3 under addition)
$\mathcal{H}, \mathcal{H}_p$	Set of dual quaternions and pure dual quaternions (the latter is isomorphic to \mathbb{R}^6 under addition)
$\mathbb{S}^3, \mathcal{S}$	Set of unit quaternions and unit dual quaternions
$\mathbf{p} \in \mathbb{H}_p$	position of a point in space with known first order kinematics
$\underline{l} \in \mathcal{H}_p \cap \mathcal{S}$	line in space with known first order kinematics
$\boldsymbol{\pi}$	plane in space with known first order kinematics
$\mathbf{q} \in \mathbb{R}^n$	vector of joints' configurations
$\mathbf{J}_\# \in \mathbb{R}^{m \times n}$	Jacobian relating joint velocities and an m -degrees-of-freedom task $\#$
$\mathbf{t} \in \mathbb{H}_p$	position of a point in the robot
$\mathbf{r} \in \mathbb{S}^3$	orientation of a frame in the robot
$\mathbf{x} \in \mathcal{S}$	pose of a frame in the robot
$\underline{l}_z \in \mathcal{H}_p \cap \mathcal{S}$	line passing through the z -axis of a frame in the robot
$d_{\#1, \#2}$	distance function between geometric entities $\#1$ and $\#2$
$D_{\#1, \#2}$	squared distance between geometric entities $\#1$ and $\#2$
η	task-space proportional gain
η_d, η_D	gains for the distance or squared distance constraints

The proposed virtual fixtures framework makes extensive use of dual quaternion algebra thanks to its several advantages over other representations. For instance, unit dual quaternions do not have representational singularities and are more compact and computationally efficient than homogeneous transformation matrices [29]. Their strong algebraic properties allow different robots to be systematically modeled [29]–[32]. Furthermore, dual quaternions can be used to represent rigid motions, twists, wrenches and several geometrical

primitives—e.g., Plücker lines, planes, cylinders—in a very straightforward way [33]. The next subsection introduces the basic definitions of quaternions and dual quaternions; more information can be found in [30], [33], [34].

A. Quaternions and Dual Quaternions

Quaternions can be regarded as an extension of complex numbers. The quaternion set is

$$\mathbb{H} \triangleq \left\{ h_1 + \hat{i}h_2 + \hat{j}h_3 + \hat{k}h_4 : h_1, h_2, h_3, h_4 \in \mathbb{R} \right\},$$

in which the imaginary units \hat{i} , \hat{j} , and \hat{k} have the following properties: $\hat{i}^2 = \hat{j}^2 = \hat{k}^2 = \hat{i}\hat{j}\hat{k} = -1$. The dual quaternion set is

$$\mathcal{H} \triangleq \{ \mathbf{h} + \varepsilon \mathbf{h}' : \mathbf{h}, \mathbf{h}' \in \mathbb{H}, \varepsilon^2 = 0, \varepsilon \neq 0 \},$$

where ε is the dual (or Clifford) unit [34]. Addition and multiplication are defined for dual quaternions analogously to complex numbers, hence we just need to respect the properties of the imaginary and dual units.

Given $\underline{\mathbf{h}} \in \mathcal{H}$ such that $\underline{\mathbf{h}} = h_1 + \hat{i}h_2 + \hat{j}h_3 + \hat{k}h_4 + \varepsilon (h'_1 + \hat{i}h'_2 + \hat{j}h'_3 + \hat{k}h'_4)$, we define the operators

$$\mathcal{P}(\underline{\mathbf{h}}) \triangleq h_1 + \hat{i}h_2 + \hat{j}h_3 + \hat{k}h_4, \quad \mathcal{D}(\underline{\mathbf{h}}) \triangleq h'_1 + \hat{i}h'_2 + \hat{j}h'_3 + \hat{k}h'_4,$$

and

$$\text{Re}(\underline{\mathbf{h}}) \triangleq h_1 + \varepsilon h'_1,$$

$$\text{Im}(\underline{\mathbf{h}}) \triangleq \hat{i}h_2 + \hat{j}h_3 + \hat{k}h_4 + \varepsilon (\hat{i}h'_2 + \hat{j}h'_3 + \hat{k}h'_4).$$

The conjugate of $\underline{\mathbf{h}}$ is $\underline{\mathbf{h}}^* \triangleq \text{Re}(\underline{\mathbf{h}}) - \text{Im}(\underline{\mathbf{h}})$, and its norm is given by $\|\underline{\mathbf{h}}\| = \sqrt{\underline{\mathbf{h}}\underline{\mathbf{h}}^*} = \sqrt{\mathbf{h}^*\mathbf{h}}$.

The set $\mathbb{H}_p \triangleq \{ \mathbf{h} \in \mathbb{H} : \text{Re}(\mathbf{h}) = 0 \}$ has a bijective relation with \mathbb{R}^3 . This way, the quaternion $(x\hat{i} + y\hat{j} + z\hat{k}) \in \mathbb{H}_p$ represents the point $(x, y, z) \in \mathbb{R}^3$. The set of quaternions with unit norm is $\mathbb{S}^3 \triangleq \{ \mathbf{h} \in \mathbb{H} : \|\mathbf{h}\| = 1 \}$, and $\mathbf{r} \in \mathbb{S}^3$ can always be written as $\mathbf{r} = \cos(\phi/2) + \mathbf{v} \sin(\phi/2)$, where $\phi \in \mathbb{R}$ is the rotation angle around the rotation axis $\mathbf{v} \in \mathbb{S}^3 \cap \mathbb{H}_p$ [33]. Elements of the set $\mathcal{S} \triangleq \{ \underline{\mathbf{h}} \in \mathcal{H} : \|\underline{\mathbf{h}}\| = 1 \}$ are called unit dual quaternions and represent tridimensional poses (i.e., combined position and orientation) of rigid bodies. Given $\underline{\mathbf{x}} \in \mathcal{S}$, it can always be written as $\underline{\mathbf{x}} = \mathbf{r} + \varepsilon(1/2)\mathbf{tr}$, where $\mathbf{r} \in \mathbb{S}^3$ and $\mathbf{t} \in \mathbb{H}_p$ represent the orientation and position, respectively [34]. The set \mathcal{S} equipped with the multiplication operation forms the group $\text{Spin}(3) \times \mathbb{R}^3$, which double covers $\text{SE}(3)$.

Elements of the set $\mathcal{H}_p \triangleq \{ \underline{\mathbf{h}} \in \mathcal{H} : \text{Re}(\underline{\mathbf{h}}) = 0 \}$ are called pure dual quaternions. Given $\underline{\mathbf{a}}, \underline{\mathbf{b}} \in \mathcal{H}_p$, the inner product and the cross product are respectively [30], [33]

$$\langle \underline{\mathbf{a}}, \underline{\mathbf{b}} \rangle \triangleq -\frac{\underline{\mathbf{a}}\underline{\mathbf{b}} + \underline{\mathbf{b}}\underline{\mathbf{a}}}{2}, \quad \underline{\mathbf{a}} \times \underline{\mathbf{b}} \triangleq \frac{\underline{\mathbf{a}}\underline{\mathbf{b}} - \underline{\mathbf{b}}\underline{\mathbf{a}}}{2}. \quad (1)$$

The operator vec_4 maps quaternions into \mathbb{R}^4 and vec_8 maps dual quaternions into \mathbb{R}^8 . For instance, $\text{vec}_4 \underline{\mathbf{h}} \triangleq [h_1 \ h_2 \ h_3 \ h_4]^T$ and $\text{vec}_8 \underline{\mathbf{h}} \triangleq [h_1 \ h_2 \ h_3 \ h_4 \ h'_1 \ h'_2 \ h'_3 \ h'_4]^T$.

Given $\mathbf{h}_1, \mathbf{h}_2 \in \mathbb{H}$, the Hamilton operators are matrices that satisfy $\text{vec}_4(\mathbf{h}_1\mathbf{h}_2) = \overset{+}{\mathbf{H}}_4(\mathbf{h}_1) \text{vec}_4 \mathbf{h}_2 = \overset{-}{\mathbf{H}}_4(\mathbf{h}_2) \text{vec}_4 \mathbf{h}_1$.

Analogously, given $\underline{h}_1, \underline{h}_2 \in \mathcal{H}$, the Hamilton operators satisfy $\text{vec}_8(\underline{h}_1 \underline{h}_2) = \bar{\mathbf{H}}_8(\underline{h}_1) \text{vec}_8 \underline{h}_2 = \bar{\mathbf{H}}_8(\underline{h}_2) \text{vec}_8 \underline{h}_1$ [33].

From (1), one can find by direct calculation that the inner product of any two pure quaternions $\mathbf{a} = \hat{i}a_2 + \hat{j}a_3 + \hat{k}a_4$ and $\mathbf{b} = \hat{i}b_2 + \hat{j}b_3 + \hat{k}b_4$ is a real number given by

$$\langle \mathbf{a}, \mathbf{b} \rangle = -\frac{\mathbf{ab} + \mathbf{ba}}{2} = \text{vec}_4 \mathbf{a}^T \text{vec}_4 \mathbf{b} = \text{vec}_4 \mathbf{b}^T \text{vec}_4 \mathbf{a}. \quad (2)$$

Furthermore, the cross product between \mathbf{a} and \mathbf{b} is mapped into \mathbb{R}^4 as

$$\begin{aligned} \text{vec}_4(\mathbf{a} \times \mathbf{b}) &= \underbrace{\begin{bmatrix} 0 & 0 & 0 & 0 \\ 0 & 0 & -a_4 & a_3 \\ 0 & a_4 & 0 & -a_2 \\ 0 & -a_3 & a_2 & 0 \end{bmatrix}}_{\bar{\mathbf{S}}(\mathbf{a})} \text{vec}_4 \mathbf{b} \\ &= \bar{\mathbf{S}}(\mathbf{a}) \text{vec}_4 \mathbf{b} = \bar{\mathbf{S}}(\mathbf{b})^T \text{vec}_4 \mathbf{a}. \end{aligned} \quad (3)$$

When it exists, the time-derivative of the squared norm of a time-varying quaternion $\mathbf{h}(t) \in \mathbb{H}_p$ is given by

$$\frac{d}{dt} (\|\mathbf{h}\|^2) = \dot{\mathbf{h}}\mathbf{h}^* + \mathbf{h}\dot{\mathbf{h}}^* = 2\langle \dot{\mathbf{h}}, \mathbf{h} \rangle. \quad (4)$$

B. Differential kinematics

Differential kinematics is the relation between task space velocities and joint space velocities, in the general form $\dot{\mathbf{x}} = \mathbf{J}\dot{\mathbf{q}}$, in which $\mathbf{q} \triangleq \mathbf{q}(t) \in \mathbb{R}^n$ is the vector of manipulator joints' configurations, $\mathbf{x} \triangleq \mathbf{x}(\mathbf{q}) \in \mathbb{R}^m$ is the vector of m task-space variables, and $\mathbf{J} \triangleq \mathbf{J}(\mathbf{q}) \in \mathbb{R}^{m \times n}$ is a Jacobian matrix.

For instance, given the robot end-effector pose $\underline{\mathbf{x}} \triangleq \underline{\mathbf{x}}(\mathbf{q}) \in \text{Spin}(3) \times \mathbb{R}^3$, the differential kinematics is given by

$$\text{vec}_8 \dot{\underline{\mathbf{x}}} = \mathbf{J}_{\underline{\mathbf{x}}} \dot{\mathbf{q}}, \quad (5)$$

where $\mathbf{J}_{\underline{\mathbf{x}}} \in \mathbb{R}^{8 \times n}$ is the dual quaternion analytical Jacobian, which can be found using dual quaternion algebra [29]. Similarly, given the end effector position $\mathbf{t} \triangleq \mathbf{t}(\mathbf{q}) \in \mathbb{H}_p$ and the end effector orientation $\mathbf{r} \triangleq \mathbf{r}(\mathbf{q}) \in \mathbb{S}^3$, such that $\underline{\mathbf{x}} = \mathbf{r} + \varepsilon(1/2)\mathbf{tr}$, we have

$$\text{vec}_4 \dot{\mathbf{t}} = \mathbf{J}_t \dot{\mathbf{q}}, \quad (6)$$

$$\text{vec}_4 \dot{\mathbf{r}} = \mathbf{J}_r \dot{\mathbf{q}}, \quad (7)$$

where $\mathbf{J}_t, \mathbf{J}_r \in \mathbb{R}^{4 \times n}$ are also calculated from $\mathbf{J}_{\underline{\mathbf{x}}}$ using dual quaternion algebra [35]. In general applications, $\underline{\mathbf{x}}, \mathbf{t}$, and \mathbf{r} are not restricted to the end effector, and may refer to any point kinematically coupled to the robot.

In this paper, points, lines, and planes kinematically coupled to the robot are called *robot entities*.

C. Quadratic programming for differential inverse kinematics

In closed-loop differential inverse kinematics, we first define a task space target, \mathbf{x}_d , and a task error $\tilde{\mathbf{x}} = \mathbf{x} - \mathbf{x}_d$. Considering $\dot{\mathbf{x}}_d = \mathbf{0}, \forall t$, and a gain $\eta \in (0, \infty)$, the analytical solution to the convex optimization problem [36]

$$\min_{\dot{\mathbf{q}}} \|\mathbf{J}\dot{\mathbf{q}} + \eta\tilde{\mathbf{x}}\|_2^2, \quad (8)$$

is the set of minimizers²

$$Q \triangleq \left\{ \dot{\mathbf{q}}^o \in \mathbb{R}^n : \dot{\mathbf{q}}^o = -\mathbf{J}^\dagger \eta \tilde{\mathbf{x}} + (\mathbf{I} - \mathbf{J}^\dagger \mathbf{J}) \mathbf{z} \right\},$$

in which \mathbf{J}^\dagger is the Moore-Penrose inverse of \mathbf{J} , \mathbf{I} is an identity matrix of proper size, and $\mathbf{z} \in \mathbb{R}^n$ is an arbitrary vector. In special, the analytical solution $\dot{\mathbf{q}}^o = -\mathbf{J}^\dagger \eta \tilde{\mathbf{x}}$ is the solution to the following optimization problem

$$\min_{\dot{\mathbf{q}} \in Q} \|\dot{\mathbf{q}}\|_2^2. \quad (9)$$

Adding linear constraints to Problem 8 turns it into a linearly constrained quadratic programming problem requiring a numerical solver [37]. The standard form of Problem 8 with *linear* constraints is

$$\begin{aligned} \min_{\dot{\mathbf{q}}} \|\mathbf{J}\dot{\mathbf{q}} + \eta\tilde{\mathbf{x}}\|_2^2 \\ \text{subject to } \mathbf{W}\dot{\mathbf{q}} \preceq \mathbf{w}, \end{aligned} \quad (10)$$

in which $\mathbf{W} \triangleq \mathbf{W}(\mathbf{q}) \in \mathbb{R}^{r \times n}$ and $\mathbf{w} \triangleq \mathbf{w}(\mathbf{q}) \in \mathbb{R}^r$. Problem 10 is the optimization of a convex quadratic function, since $\mathbf{J}^T \mathbf{J} \geq 0$ over the polyhedron $\mathbf{W}\dot{\mathbf{q}} \preceq \mathbf{w}$ [36]. Furthermore, Problem 10 does not limit the joint velocity norm, hence it may generate unfeasible velocities. To avoid a nested optimization such as in Problem 9—which requires a higher computational time—we resort to adding a damping factor $\lambda \in [0, \infty)$ to Problem 10 to find

$$\min_{\dot{\mathbf{q}}} \|\mathbf{J}\dot{\mathbf{q}} + \eta\tilde{\mathbf{x}}\|_2^2 + \lambda \|\dot{\mathbf{q}}\|_2^2 \quad (11)$$

subject to $\mathbf{W}\dot{\mathbf{q}} \preceq \mathbf{w}$,

which limits joint velocity norm.

More than one robot can be controlled simultaneously with Problem 11 in a centralized architecture, which is suitable for most applications in surgical robotics. Suppose that p robots should follow their own independent task space trajectories. For $i = 1, \dots, p$, let each robot R_i have n_i joints, joint velocity vector $\dot{\mathbf{q}}_i$, task Jacobian \mathbf{J}_i , and task error $\tilde{\mathbf{x}}_i$. Problem 10 becomes

$$\min_{\dot{\mathbf{g}}} \|\mathbf{A}\dot{\mathbf{g}} + \eta\tilde{\mathbf{y}}\|_2^2 + \lambda \|\dot{\mathbf{g}}\|_2^2 \quad (12)$$

subject to $\mathbf{M}\dot{\mathbf{g}} \preceq \mathbf{m}$,

in which

$$\mathbf{A} = \begin{bmatrix} \mathbf{J}_1 & \cdots & \mathbf{0} \\ \vdots & \ddots & \vdots \\ \mathbf{0} & \cdots & \mathbf{J}_p \end{bmatrix}, \quad \mathbf{g} = \begin{bmatrix} \mathbf{q}_1 \\ \vdots \\ \mathbf{q}_p \end{bmatrix}, \quad \tilde{\mathbf{y}} = \begin{bmatrix} \tilde{\mathbf{x}}_1 \\ \vdots \\ \tilde{\mathbf{x}}_p \end{bmatrix},$$

$\mathbf{M} \triangleq \mathbf{M}(\mathbf{g}) \in \mathbb{R}^{r \times \sum n_i}$, $\mathbf{m} \triangleq \mathbf{m}(\mathbf{g}) \in \mathbb{R}^r$, and $\mathbf{0}$ is a matrix of zeros with appropriate dimensions.

The vector field inequalities proposed in Section III use appropriate linear constraints to generate dynamic active constraints. In addition, by solving Problem 12, we locally ensure the smallest trajectory tracking error for a collision-free path.

²In optimization literature (e.g. [36]), a minimizer is usually denoted with a superscript asterisk, such as $\dot{\mathbf{q}}^*$. However, we use the superscript o , as in $\dot{\mathbf{q}}^o$, to avoid notational confusions with the dual-quaternion conjugate.

In this work we assume that the desired trajectory, $x_d(t)$, is generated online by the surgeon, may it be through teleoperation or co-manipulation. In this case, trajectory tracking controllers that require future knowledge of the trajectory [38] cannot be used, and a set-point regulator given by the solution of Problem 12 is a proper choice.

III. VECTOR FIELD INEQUALITY FOR DYNAMIC ENTITIES

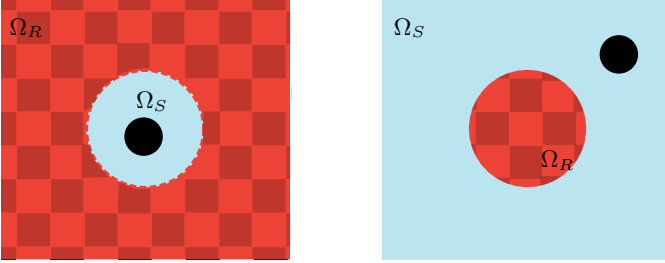


Fig. 1. The proposed vector field inequalities can have two types of behavior, in which the black circle represents a robot entity: keeping a robot entity inside a safe zone, Ω_S (left); or outside of a restricted zone, Ω_R (right). Restricted zones are checked for contrast with safe zones.

The vector field inequality for dynamic elements requires:

- 1) A function $d \triangleq d(\mathbf{q}, t) \in \mathbb{R}$ that encodes the (signed) distance between the two collidable entities. The *robot entity* is kinematically coupled to the robot, and the other entity, called *restricted zone*, is part of the workspace (or part of another robot);
- 2) A Jacobian relating the time derivative of the distance function and the joints' velocities in the general form

$$\dot{d} = \underbrace{\frac{\partial(d(\mathbf{q}, t))}{\partial \mathbf{q}}}_{\mathbf{J}_d} \dot{\mathbf{q}} + \zeta(t), \quad (13)$$

in which the residual $\zeta(t) = \dot{d} - \mathbf{J}_d \dot{\mathbf{q}}$ contains the distance dynamics unrelated to the joints' velocities.

We assume that the residual is known but it cannot be controlled. For instance, the residual might encode the movement of a geometrical entity, which can be related to the workspace, that can be tracked or estimated.³

Using distance functions and distance Jacobians, complex dynamic restricted zones can be generated, either by maintaining the distance above a desired level or by keeping the distance below a certain level, as illustrated in Fig. 1.

A. Keeping the robot entity outside a restricted region

To keep the robot entity outside of a restricted zone, we define a minimum safe distance $d_{\text{safe}} \triangleq d_{\text{safe}}(t) \in [0, \infty)$, which delineates the time-dependent boundary of the restricted zone, and a signed distance

$$\tilde{d} \triangleq \tilde{d}(\mathbf{q}, t) = d - d_{\text{safe}}. \quad (14)$$

³The vector field inequalities proposed in our earlier work [28] is a special case of the framework proposed in this work with $\zeta(t) = 0, \forall t$.

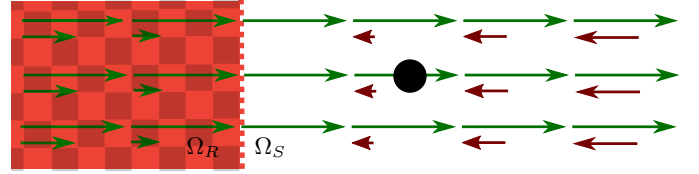


Fig. 2. A vector field inequality that keeps a point outside of the restricted zone, Ω_R , whose boundary is a plane. To each point in space is assigned a maximum approach velocity (the lower vector in each vector pair), and a maximum separation velocity (the upper vector in each vector pair). The approach velocity decreases exponentially with the distance, and the maximum separating velocity is unconstrained.

The restricted zone Ω_R and the safe zone Ω_S are

$$\begin{aligned} \Omega_R &\triangleq \left\{ \mathbf{q} \in \mathbb{R}^n, t \in [0, \infty) : \tilde{d}(\mathbf{q}, t) < 0 \right\}, \\ \Omega_S &\triangleq \left\{ \mathbf{q} \in \mathbb{R}^n, t \in [0, \infty) : \tilde{d}(\mathbf{q}, t) \geq 0 \right\}. \end{aligned}$$

The signed distance dynamics is given by

$$\dot{\tilde{d}} = \dot{d} - \dot{d}_{\text{safe}}. \quad (15)$$

A positive $\dot{\tilde{d}}$ means that the robot entity and the restricted zone are moving away from each other, whereas a negative $\dot{\tilde{d}}$ means that they are moving closer to each other.

Given $\eta_d \in [0, \infty)$, the signed distance dynamics is constrained by [26]

$$\dot{\tilde{d}} \geq -\eta_d \tilde{d}. \quad (16)$$

Constraint 16 assigns to each point in space a velocity constraint for the robot entity—as illustrated in Fig. 2—, which has at least exponential behavior according to the Gronwall's lemma [27]. To understand the physical meaning of the constraint, first suppose that $\tilde{d}(\mathbf{q}, 0) \geq 0$, which means that the robot entity is in the safe zone when $t = 0$. In this situation, any increase in distance is *always* allowed, which implies $\dot{\tilde{d}} \geq 0 \geq -\eta_d \tilde{d}$. However, when the distance decreases, $0 \geq \dot{\tilde{d}} \geq -\eta_d \tilde{d}$ and the *maximum* distance decrease rate is exponential, given by $\dot{\tilde{d}} = -\eta_d \tilde{d}$. This way, as the robot entity comes closer to the restricted zone, the allowed approach velocity between the restricted zone and the system gets smaller. Any slower approaching motion is also allowed, hence $\dot{\tilde{d}} \geq -\eta_d \tilde{d}$. As soon as $\tilde{d} = 0$, the restriction becomes $\dot{\tilde{d}} \geq 0$ and therefore the robot entity will not enter the restricted zone.

Now consider that $\tilde{d}(\mathbf{q}, 0) < 0$; that is, the system starts inside the restricted zone. In this case, Constraint 16 will only be fulfilled if $\dot{\tilde{d}} \geq \eta_d |\tilde{d}|$, which means that the system will, at least, be pushed towards the safe zone with *minimum* distance decrease rate given by $\dot{\tilde{d}} = -\eta_d \tilde{d} = \eta_d |\tilde{d}|$.

Using (13) and (15), Constraint 16 is written explicitly in terms of joint velocities as

$$\mathbf{J}_d \dot{\mathbf{q}} \geq -\eta_d \tilde{d} - \zeta_{\text{safe}}(t), \quad (17)$$

where the residual $\zeta_{\text{safe}}(t) \triangleq \zeta(t) - \dot{d}_{\text{safe}}$ takes into account the effects, on the distance, of a moving obstacle with residual $\zeta(t)$ and of a time-varying safe-zone boundary \dot{d}_{safe} . If $\zeta_{\text{safe}} >$

0, the restricted zone contributes⁴ to an increase in the distance between itself and the robot entity. Conversely, if $\zeta_{\text{safe}} < 0$, then the restricted zone contributes to a decrease in the distance between itself and the robot entity. If $\zeta_{\text{safe}} + \eta_d \tilde{d} < 0$, then the robot has to actively move away from the restricted zone.

To fit into Problem 12, we rewrite Constraint 17 as

$$- \mathbf{J}_d \dot{\mathbf{q}} \leq \eta_d \tilde{d} + \zeta_{\text{safe}}(t). \quad (18)$$

Notice that any number of constraints in the form of Constraint 18 can be found for different interactions between robot entities and restricted zones in the robot workspace. Moreover, by describing the interaction as a distance function, complex interactions will be only one degree-of-freedom constraints.

Remark 1. When the distance is obtained using the Euclidean norm, its derivative is singular when the norm is zero. The squared distance is useful to avoid such singularities, as shown in Sections IV-C and IV-E. When the squared distance $D \triangleq d^2$ is used, the signed distance (14) is redefined as $\tilde{D} \triangleq \tilde{D}(\mathbf{q}, t) = D - D_{\text{safe}}$ in which $D_{\text{safe}} \triangleq d_{\text{safe}}^2$ [35]. Constraint 16 then becomes $\dot{\tilde{D}} \geq -\eta_D \tilde{D}$, and any reasoning is otherwise unaltered.

B. Keeping the robot entity inside a safe region

Using the same methodology of Subsection III-A, we re-define d_{safe} to maintain the robot *inside* a safe region; that is,

$$\tilde{d} \triangleq d_{\text{safe}} - d,$$

with final solution, assuming the desired signed distance dynamics (16), given by

$$\mathbf{J}_d \dot{\mathbf{q}} \leq \eta_d \tilde{d} - \zeta_{\text{safe}}. \quad (19)$$

IV. SQUARED DISTANCE FUNCTIONS AND CORRESPONDING JACOBIANS

In order to use the vector field inequalities (18) and (19), we define (squared) distance functions for relevant geometrical primitives (point, line, and plane) and then we find the corresponding Jacobians and residuals. These geometrical primitives can be easily combined to obtain other primitives. For instance, a point combined with a positive scalar yields a sphere, whereas a line combined with a positive scalar yields an infinite cylinder; the intersection between an infinite cylinder and two parallel planes results in a finite cylinder; polyhedra can be defined as intersections of planes. Table II summarizes the distance functions and corresponding Jacobians.

A. Manipulator point-to-point squared distance $D_{t,p}$ and Jacobian $\mathbf{J}_{t,p}$

The Euclidean distance between two points $\mathbf{p}_1, \mathbf{p}_2 \in \mathbb{H}_p$ is given by⁵

$$d_{\mathbf{p}_1, \mathbf{p}_2} = \|\mathbf{p}_1 - \mathbf{p}_2\|. \quad (20)$$

⁴The motion of the restricted zone takes into account the actual obstacle motion and the motion of the safe boundary (i.e., when $\dot{d}_{\text{safe}} \neq 0$).

⁵The quaternion norm is equivalent to the Euclidean norm.

TABLE II
SUMMARY OF PRIMITIVES

Primitive	Distance function	Jacobian	Residual
Point-to-Point	$D_{t,p}$ (Eq. 21)	$\mathbf{J}_{t,p}$ (Eq. 22)	$\zeta_{t,p}$ (Eq. 22)
Point-to-Line	$D_{t,l}$ (Eq. 29)	$\mathbf{J}_{t,l}$ (Eq. 32)	$\zeta_{t,l}$ (Eq. 32)
Line-to-Point	$D_{l,p}$ (Eq. 33)	$\mathbf{J}_{l,p}$ (Eq. 34)	$\zeta_{l,p}$ (Eq. 34)
Line-to-Line	$D_{l_z,l}$ (Eq. 50)	$\mathbf{J}_{l_z,l}$ (Eq. 48)	$\zeta_{l_z,l}$ (Eq. 49)
Plane-to-Point	$d_{\pi_z,p}^{\pi}$ (Eq. 54)	$\mathbf{J}_{\pi_z,p}$ (Eq. 56)	$\zeta_{\pi_z,p}$ (Eq. 55)
Point-to-Plane	$d_{t,\pi}^{\pi}$ (Eq. 57)	$\mathbf{J}_{t,\pi}$ (Eq. 59)	ζ_{π} (Eq. 58)

Since the time derivative of (20) is singular at $d = 0$ [35], we use the squared distance, whose time derivative is defined everywhere:

$$D_{\mathbf{p}_1, \mathbf{p}_2} \triangleq d_{\mathbf{p}_1, \mathbf{p}_2}^2 = \|\mathbf{p}_1 - \mathbf{p}_2\|^2. \quad (21)$$

Given a point $\mathbf{t} \triangleq \mathbf{t}(\mathbf{q}(t)) \in \mathbb{H}_p$ in the robot, where $\mathbf{q}(t) \in \mathbb{R}^n$ is the time-varying joints' configuration, and an arbitrary point $\mathbf{p} \triangleq \mathbf{p}(t) \in \mathbb{H}_p$ in space, we use (4) and (6) to find

$$\frac{d}{dt}(D_{t,p}) = 2 \underbrace{\text{vec}_4(\mathbf{t} - \mathbf{p})^T \mathbf{J}_t \dot{\mathbf{q}}}_{\mathbf{J}_{t,p}} + 2 \underbrace{\langle \mathbf{t} - \mathbf{p}, -\dot{\mathbf{p}} \rangle}_{\zeta_{t,p}}. \quad (22)$$

B. The dual quaternion line \underline{l}_z and line Jacobian \mathbf{J}_{l_z}

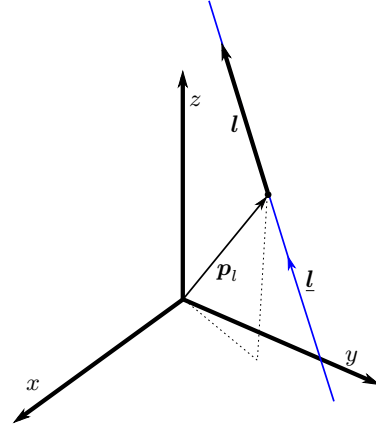


Fig. 3. Representation of a Plücker line $\underline{l} \triangleq l + \epsilon m$, where l is the line direction, $m = \mathbf{p}_l \times l$ is the line moment, and \mathbf{p}_l is an arbitrary point in the line.

In minimally invasive surgery and microsurgery, tools have long and thin shafts, which may have some parts outside of the field-of-view; therefore, collisions with other tools or the environment might happen. By describing tool-shafts using Plücker lines, such interactions can be mathematically modeled. A Plücker line (see Fig. 3) belongs to the set $\mathcal{H}_p \cap \underline{\mathcal{S}}$, and thus is represented by a unit dual quaternion such as [30], [33]

$$\underline{l} = l + \epsilon m, \quad (23)$$

where $l \in \mathbb{H}_p \cap \mathbb{S}^3$ is a pure quaternion with unit norm that represents the line direction, and the line moment is given by $m = \mathbf{p}_l \times l$, in which $\mathbf{p}_l \in \mathbb{H}_p$ is an arbitrary point in the line.

When the robot forward kinematics is described using the Denavit-Hartenberg convention, the z -axis of each frame

passes through the corresponding joint actuation axis [9].⁶ Hence, it is specially useful to find the Jacobian relating joint velocities and the line that passes through the z -axis of a reference frame in the robot.

Consider a Plücker line on top of the z -axis of a frame of interest, whose pose is given by $\underline{x} = \mathbf{r} + \frac{1}{2}\varepsilon\mathbf{t}\mathbf{r}$, in a robotic manipulator kinematic chain. Since the frame of interest changes according to the robot motion, the line changes accordingly, hence

$$\underline{l}_z \triangleq \underline{l}_z(\mathbf{q}(t)) = \mathbf{l}_z + \varepsilon\mathbf{m}_z, \quad (24)$$

where $\mathbf{l}_z = \hat{\mathbf{r}}\hat{\mathbf{k}}\mathbf{r}^*$ and $\mathbf{m}_z = \mathbf{t} \times \mathbf{l}_z$. The derivative of (24) is

$$\dot{\underline{l}}_z = \dot{\mathbf{l}}_z + \varepsilon\dot{\mathbf{m}}_z, \quad (25)$$

where $\dot{\mathbf{l}}_z = \dot{\mathbf{r}}\hat{\mathbf{k}}\mathbf{r}^* + \mathbf{r}\hat{\mathbf{k}}\dot{\mathbf{r}}^*$, thus

$$\text{vec}_4 \dot{\underline{l}}_z = \underbrace{\left(\bar{\mathbf{H}}_4(\hat{\mathbf{k}}\mathbf{r}^*) \mathbf{J}_r + \bar{\mathbf{H}}_4(\mathbf{r}\hat{\mathbf{k}}) \mathbf{C}_4 \mathbf{J}_r \right)}_{\mathbf{J}_{r_z}} \dot{\mathbf{q}}, \quad (26)$$

in which $\mathbf{C}_4 = \text{diag}(1, -1, -1, -1)$ and $\text{vec}_4 \dot{\mathbf{r}}$ is given by (7); in addition, the derivative of the line moment is $\dot{\mathbf{m}}_z = \dot{\mathbf{t}} \times \mathbf{l}_z + \mathbf{t} \times \dot{\mathbf{l}}_z$, hence we use (3), (6), and (26) to obtain

$$\text{vec}_4 \dot{\mathbf{m}}_z = \underbrace{\left(\bar{\mathbf{S}}(\mathbf{l}_z)^T \mathbf{J}_t + \bar{\mathbf{S}}(\mathbf{t}) \mathbf{J}_{r_z} \right)}_{\mathbf{J}_{m_z}} \dot{\mathbf{q}}. \quad (27)$$

Finally, we rewrite (25) explicitly in term of joint-velocities using (26) and (27) as

$$\text{vec}_8 \dot{\underline{l}}_z = \begin{bmatrix} \mathbf{J}_{r_z} \\ \mathbf{J}_{m_z} \end{bmatrix} \dot{\mathbf{q}} \triangleq \mathbf{J}_{l_z} \dot{\mathbf{q}}. \quad (28)$$

C. Manipulator point-to-line squared distance $D_{t,l}$ and Jacobian $\mathbf{J}_{t,l}$

Considering the robot joints' configuration vector $\mathbf{q}(t) \in \mathbb{R}^n$ and a point $\mathbf{t} \triangleq \mathbf{t}(\mathbf{q}(t)) \in \mathbb{H}_p$ in the robot, the squared distance between \mathbf{t} and a arbitrary line $\underline{l} \triangleq \underline{l}(t) \in \mathcal{H}_p \cap \underline{\mathcal{S}}$ in space is given by [39]

$$D_{t,l} \triangleq \|\mathbf{t} \times \mathbf{l} - \mathbf{m}\|^2. \quad (29)$$

For notational convenience we define $\mathbf{h}_{A1} \triangleq \mathbf{t} \times \mathbf{l} - \mathbf{m}$, whose derivative is

$$\dot{\mathbf{h}}_{A1} = \dot{\mathbf{t}} \times \mathbf{l} + \underbrace{\mathbf{t} \times \dot{\mathbf{l}} - \dot{\mathbf{m}}}_{\mathbf{h}_{A2}}. \quad (30)$$

Using (2), (3), (4), and 30, we obtain

$$\begin{aligned} \dot{D}_{t,l} &= 2\langle \dot{\mathbf{h}}_{A1}, \mathbf{h}_{A1} \rangle \\ &= 2\langle (\dot{\mathbf{t}} \times \mathbf{l}), \mathbf{h}_{A1} \rangle + 2\langle \mathbf{h}_{A2}, \mathbf{h}_{A1} \rangle \\ &= 2\text{vec}_4(\mathbf{h}_{A1})^T \bar{\mathbf{S}}(\mathbf{l})^T \text{vec}_4(\dot{\mathbf{t}}) + 2\langle \mathbf{h}_{A2}, \mathbf{h}_{A1} \rangle. \end{aligned} \quad (31)$$

Letting $\zeta_{t,l} \triangleq 2\langle \mathbf{h}_{A2}, \mathbf{h}_{A1} \rangle$, we use (6) to obtain the squared-distance time derivative explicitly in terms of the robot joints' velocities:

$$\dot{D}_{t,l} = 2\text{vec}_4(\mathbf{t} \times \mathbf{l} - \mathbf{m})^T \underbrace{\bar{\mathbf{S}}(\mathbf{l})^T \mathbf{J}_t}_{\mathbf{J}_{t,l}} \dot{\mathbf{q}} + \zeta_{t,l}. \quad (32)$$

⁶The method described here is general enough and different conventions can be used (for instance, the joint actuation axis could be the x - or the y -axis), such that the derivation of the corresponding equations follows the same procedure.

D. Manipulator line-to-point squared distance $D_{l_z,p}$ and Jacobian $\mathbf{J}_{l_z,p}$

Given the line \underline{l}_z , as in (24), on top of the z -axis of a frame rigidly attached to the robot and an arbitrary point $\mathbf{p} \in \mathbb{H}_p$ in space, we use (29) to obtain

$$D_{l_z,p} = \|\mathbf{p} \times \mathbf{l}_z - \mathbf{m}_z\|^2. \quad (33)$$

Similarly to (32), we write the time derivative of 33 explicitly in terms of the joints' velocities:

$$\begin{aligned} \dot{D}_{l_z,p} &= 2\text{vec}_4(\mathbf{p} \times \mathbf{l}_z - \mathbf{m}_z)^T \underbrace{(\bar{\mathbf{S}}(\mathbf{p}) \mathbf{J}_{l_z} - \mathbf{J}_{m_z})}_{\mathbf{J}_{l_z,p}} \dot{\mathbf{q}} \\ &\quad + 2\langle \underbrace{\dot{\mathbf{p}} \times \mathbf{l}_z, \mathbf{p} \times \mathbf{l}_z - \mathbf{m}_z}_{\zeta_{l_z,p}} \rangle. \end{aligned} \quad (34)$$

This primitive (i.e., the function $D_{l_z,p}$ together with its derivative $\dot{D}_{l_z,p}$) is useful to define a compliant remote center-of-motion by having a nonzero safe distance.

E. Manipulator line-to-line distance D_{l_1,l_2} and Jacobian \mathbf{J}_{l_1,l_2}

The distance between two Plücker lines $\underline{l}_1, \underline{l}_2 \in \mathcal{H}_p \cap \underline{\mathcal{S}}$ is obtained through inner and cross product operations. The inner product between \underline{l}_1 and \underline{l}_2 is [30]⁷

$$\begin{aligned} \langle \underline{l}_1, \underline{l}_2 \rangle &= \|\underline{l}_1\| \|\underline{l}_2\| \cos(\phi_{1,2} + \varepsilon d_{1,2}) \\ &= \cos \phi_{1,2} - \varepsilon \sin \phi_{1,2} d_{1,2}, \end{aligned} \quad (35)$$

where $d_{1,2} \in [0, \infty)$ and $\phi_{1,2} \in [0, 2\pi)$ are the distance and the angle between \underline{l}_1 and \underline{l}_2 , respectively. Moreover, given $\underline{s}_{1,2} \in \mathcal{H}_p \cap \underline{\mathcal{S}}$ —the line perpendicular to both \underline{l}_1 and \underline{l}_2 —such that $\underline{s}_{1,2} \triangleq \mathbf{s}_{1,2} + \varepsilon\mathbf{m}_{s_{1,2}}$, the cross product between \underline{l}_1 and \underline{l}_2 is [30]

$$\begin{aligned} \underline{l}_1 \times \underline{l}_2 &= \|\underline{l}_1\| \|\underline{l}_2\| \mathbf{s}_{1,2} \sin(\phi_{1,2} + \varepsilon d_{1,2}) \\ &= (\mathbf{s}_{1,2} + \varepsilon\mathbf{m}_{s_{1,2}}) (\sin \phi_{1,2} + \varepsilon \cos \phi_{1,2} d_{1,2}) \\ &= \mathbf{s}_{1,2} \sin \phi_{1,2} + \varepsilon (\mathbf{m}_{s_{1,2}} \sin \phi_{1,2} + \mathbf{s}_{1,2} \cos \phi_{1,2} d_{1,2}). \end{aligned} \quad (36)$$

The squared distance between \underline{l}_1 and \underline{l}_2 , when they are not parallel (i.e., $\phi_{1,2} \in (0, 2\pi) \setminus \pi$), is obtained using (35) and (36):

$$D_{1,2} \llcorner = \frac{\|\mathcal{D}(\langle \underline{l}_1, \underline{l}_2 \rangle)\|^2}{\|\mathcal{P}(\underline{l}_1 \times \underline{l}_2)\|^2} = \frac{\|d_{1,2} \sin \phi_{1,2}\|^2}{\|\mathbf{s}_{1,2} \sin \phi_{1,2}\|^2} = d_{1,2}^2, \quad (37)$$

The squared distance between \underline{l}_1 and \underline{l}_2 when they are parallel (i.e., $\phi_{1,2} \in \{0, \pi\}$) is obtained as

$$D_{1,2} \parallel \triangleq \|\mathcal{D}(\underline{l}_1 \times \underline{l}_2)\|^2 = \|\mathbf{s}_{1,2} d_{1,2}\|^2 = d_{1,2}^2. \quad (38)$$

To find the distance Jacobian and residual between a line \underline{l}_z in the robot and an arbitrary line \underline{l} in space, we begin by finding the inner product Jacobian and residual in Subsection IV-E1 and the cross product Jacobian and residual in Subsection IV-E2. Those are used in Subsection IV-E3 to find the derivative of (37), and in Subsection IV-E4 to find the derivative of (38). Finally, those are unified in the final form of the distance Jacobian and residual in Subsection IV-E5.

⁷Given a function $f: \mathbb{D} \rightarrow \mathbb{D}$, where $\mathbb{D} \triangleq \{\mathbf{h} \in \mathcal{H} : \text{Im}(\mathbf{h}) = 0\}$, it is possible to show that $f(a + \varepsilon b) = f(a) + \varepsilon b f'(a)$. For more details, see [33].

1) *Inner product Jacobian, $\mathbf{J}_{(\underline{l}_z, \underline{l})}$* : The time derivative of the inner product between $\underline{l}_z, \underline{l} \in \mathcal{H}_p \cap \underline{\mathcal{S}}$ is given by

$$\frac{d}{dt} (\langle \underline{l}_z, \underline{l} \rangle) = \langle \dot{\underline{l}}_z, \underline{l} \rangle + \langle \underline{l}_z, \dot{\underline{l}} \rangle = -\frac{1}{2} (\dot{\underline{l}}_z \underline{l} + \underline{l} \dot{\underline{l}}_z) + \underbrace{\langle \underline{l}_z, \dot{\underline{l}} \rangle}_{\zeta_{(\underline{l}_z, \underline{l})}}.$$

Hence, using (28) we obtain

$$\text{vec}_8 \frac{d}{dt} (\langle \underline{l}_z, \underline{l} \rangle) = -\frac{1}{2} \left(\overbrace{\mathbf{H}_8^-(\underline{l}) + \mathbf{H}_8^+(\underline{l})}^{\mathbf{J}_{(\underline{l}_z, \underline{l})}} \right) \mathbf{J}_{\underline{l}_z} \dot{\mathbf{q}} + \text{vec}_8 \zeta_{(\underline{l}_z, \underline{l})},$$

which can be explicitly written in terms of the primary and dual parts as

$$\begin{bmatrix} \text{vec}_4 \dot{\mathcal{P}}(\langle \underline{l}_z, \underline{l} \rangle) \\ \text{vec}_4 \dot{\mathcal{D}}(\langle \underline{l}_z, \underline{l} \rangle) \end{bmatrix} = \begin{bmatrix} \mathbf{J}_{\mathcal{P}(\langle \underline{l}_z, \underline{l} \rangle)} \\ \mathbf{J}_{\mathcal{D}(\langle \underline{l}_z, \underline{l} \rangle)} \end{bmatrix} \dot{\mathbf{q}} + \begin{bmatrix} \text{vec}_4 \mathcal{P}(\zeta_{(\underline{l}_z, \underline{l})}) \\ \text{vec}_4 \mathcal{D}(\zeta_{(\underline{l}_z, \underline{l})}) \end{bmatrix}. \quad (39)$$

2) *Cross product Jacobian, $\mathbf{J}_{\underline{l}_z \times \underline{l}}$* : The time derivative of the cross product between $\underline{l}_z, \underline{l} \in \mathcal{H}_p \cap \underline{\mathcal{S}}$ is given by

$$\frac{d}{dt} (\underline{l}_z \times \underline{l}) = \dot{\underline{l}}_z \times \underline{l} + \underline{l}_z \times \dot{\underline{l}} = \frac{1}{2} (\dot{\underline{l}}_z \underline{l} - \underline{l} \dot{\underline{l}}_z) + \underbrace{\underline{l}_z \times \dot{\underline{l}}}_{\zeta_{\underline{l}_z \times \underline{l}}}.$$

Using 28 we obtain

$$\text{vec}_8 \frac{d}{dt} (\underline{l}_z \times \underline{l}) = \frac{1}{2} \left(\overbrace{\mathbf{H}_8^-(\underline{l}) - \mathbf{H}_8^+(\underline{l})}^{\mathbf{J}_{\underline{l}_z \times \underline{l}}} \right) \mathbf{J}_{\underline{l}_z} \dot{\mathbf{q}} + \text{vec}_8 \zeta_{\underline{l}_z \times \underline{l}},$$

which can be explicitly written in terms of the primary and dual parts as

$$\begin{bmatrix} \text{vec}_4 \dot{\mathcal{P}}(\underline{l}_z \times \underline{l}) \\ \text{vec}_4 \dot{\mathcal{D}}(\underline{l}_z \times \underline{l}) \end{bmatrix} = \begin{bmatrix} \mathbf{J}_{\mathcal{P}(\underline{l}_z \times \underline{l})} \\ \mathbf{J}_{\mathcal{D}(\underline{l}_z \times \underline{l})} \end{bmatrix} \dot{\mathbf{q}} + \begin{bmatrix} \text{vec}_4 \mathcal{P}(\zeta_{\underline{l}_z \times \underline{l}}) \\ \text{vec}_4 \mathcal{D}(\zeta_{\underline{l}_z \times \underline{l}}) \end{bmatrix}. \quad (40)$$

3) *Non-parallel distance Jacobian, $\mathbf{J}_{\underline{l}_z, \underline{l} \parallel}$* : From (37), the squared distance between two non-parallel lines $\underline{l}_z, \underline{l} \in \mathcal{H}_p \cap \underline{\mathcal{S}}$ is

$$D_{\underline{l}_z, \underline{l} \parallel} = \frac{\|\mathcal{D}(\langle \underline{l}_z, \underline{l} \rangle)\|^2}{\|\mathcal{P}(\underline{l}_z \times \underline{l})\|^2}, \quad (41)$$

with time derivative given by

$$\dot{D}_{\underline{l}_z, \underline{l} \parallel} = \frac{\overbrace{1}^a}{\|\mathcal{P}(\underline{l}_z \times \underline{l})\|^2} \frac{d}{dt} (\|\mathcal{D}(\langle \underline{l}_z, \underline{l} \rangle)\|^2) - \underbrace{\frac{\|\mathcal{D}(\langle \underline{l}_z, \underline{l} \rangle)\|^2}{\|\mathcal{P}(\underline{l}_z \times \underline{l})\|^4}}_b \frac{d}{dt} (\|\mathcal{P}(\underline{l}_z \times \underline{l})\|^2). \quad (42)$$

We use (4) and (39) to obtain

$$\frac{d}{dt} (\|\mathcal{D}(\langle \underline{l}_z, \underline{l} \rangle)\|^2) = 2 \text{vec}_4 \mathcal{D}(\langle \underline{l}_z, \underline{l} \rangle)^T \overbrace{\mathbf{J}_{\mathcal{D}(\langle \underline{l}_z, \underline{l} \rangle)}}^{\mathbf{J}_{\|\mathcal{D}(\langle \underline{l}_z, \underline{l} \rangle)\|^2}} \dot{\mathbf{q}} + 2 \text{vec}_4 \mathcal{D}(\langle \underline{l}_z, \underline{l} \rangle)^T \underbrace{\text{vec}_4 \mathcal{D}(\zeta_{(\underline{l}_z, \underline{l})})}_{\zeta_{\|\mathcal{D}(\langle \underline{l}_z, \underline{l} \rangle)\|^2}}. \quad (43)$$

Similarly, we use (4) and (40) to obtain

$$\frac{d}{dt} (\|\mathcal{P}(\underline{l}_z \times \underline{l})\|^2) = 2 \text{vec}_4 \mathcal{P}(\underline{l}_z \times \underline{l})^T \overbrace{\mathbf{J}_{\mathcal{P}(\underline{l}_z \times \underline{l})}}^{\mathbf{J}_{\|\mathcal{P}(\underline{l}_z \times \underline{l})\|^2}} \dot{\mathbf{q}} + 2 \text{vec}_4 \mathcal{P}(\underline{l}_z \times \underline{l})^T \underbrace{\text{vec}_4 \mathcal{P}(\zeta_{\underline{l}_z \times \underline{l}})}_{\zeta_{\|\mathcal{P}(\underline{l}_z \times \underline{l})\|^2}}. \quad (44)$$

Finally, replacing (43) and (44) in (42) yields

$$\dot{D}_{\underline{l}_z, \underline{l} \parallel} = \left(a \overbrace{\mathbf{J}_{\|\mathcal{D}(\langle \underline{l}_z, \underline{l} \rangle)\|^2}}^{\mathbf{J}_{\underline{l}_z, \underline{l} \parallel}} + b \overbrace{\mathbf{J}_{\|\mathcal{P}(\underline{l}_z \times \underline{l})\|^2}} \right) \dot{\mathbf{q}} + \underbrace{a \zeta_{\|\mathcal{D}(\langle \underline{l}_z, \underline{l} \rangle)\|^2} + b \zeta_{\|\mathcal{P}(\underline{l}_z \times \underline{l})\|^2}}_{\zeta_{\underline{l}_z, \underline{l} \parallel}}. \quad (45)$$

4) *Parallel distance Jacobian, $\mathbf{J}_{\underline{l}_z, \underline{l} \parallel}$* : In the degenerate case where \underline{l}_z and \underline{l} are parallel, the squared distance $D_{\underline{l}_z, \underline{l} \parallel}$ is given by (38); that is,

$$D_{\underline{l}_z, \underline{l} \parallel} = \|\mathcal{D}(\underline{l}_z \times \underline{l})\|^2. \quad (46)$$

Using (4) and (40), the derivative of (46) is given by

$$\dot{D}_{\underline{l}_z, \underline{l} \parallel} = 2 \text{vec}_4 (\mathcal{D}(\underline{l}_z \times \underline{l}))^T \overbrace{\mathbf{J}_{\mathcal{D}(\underline{l}_z \times \underline{l})}}^{\mathbf{J}_{\underline{l}_z, \underline{l} \parallel}} \dot{\mathbf{q}} + 2 \text{vec}_4 (\mathcal{D}(\underline{l}_z \times \underline{l}))^T \underbrace{\text{vec}_4 \mathcal{D}(\zeta_{\underline{l}_z \times \underline{l}})}_{\zeta_{\underline{l}_z, \underline{l} \parallel}}. \quad (47)$$

5) *Manipulator line-to-line distance Jacobian, $\mathbf{J}_{\underline{l}_z, \underline{l}}$* : The line-to-line distance Jacobian and residual are given by taking into account both (45) and (47) as

$$\mathbf{J}_{\underline{l}_z, \underline{l}} = \begin{cases} \mathbf{J}_{\underline{l}_z, \underline{l} \parallel} & \phi \in (0, 2\pi) \setminus \pi \\ \mathbf{J}_{\underline{l}_z, \underline{l} \parallel} & \phi \in \{0, \pi\} \end{cases}, \quad (48)$$

$$\zeta_{\underline{l}_z, \underline{l}} = \begin{cases} \zeta_{\underline{l}_z, \underline{l} \parallel} & \phi \in (0, 2\pi) \setminus \pi \\ \zeta_{\underline{l}_z, \underline{l} \parallel} & \phi \in \{0, \pi\} \end{cases}, \quad (49)$$

in which $\phi = \arccos \mathcal{P}(\langle \underline{l}_z, \underline{l} \rangle)$.

Similarly, the distance between lines is given by taking into account both (41) and (46) as

$$D_{\underline{l}_z, \underline{l}} = \begin{cases} D_{\underline{l}_z, \underline{l} \parallel} & \phi \in (0, 2\pi) \setminus \pi \\ D_{\underline{l}_z, \underline{l} \parallel} & \phi \in \{0, \pi\} \end{cases}. \quad (50)$$

F. *Robot plane-to-point distance $d_{\pi_z, \mathbf{p}}$ and Jacobian $\mathbf{J}_{\pi_z, \mathbf{p}}$*

To obtain the required relations between a plane $\underline{\pi}$ and a point, we use the plane representation in dual quaternion space, which is given by [33]

$$\underline{\pi} \triangleq \mathbf{n}_\pi + \varepsilon d_\pi, \quad (51)$$

where $\mathbf{n}_\pi \in \mathbb{H}_p \cap \mathbb{S}^3$ is the normal to the plane and $d_\pi \in \mathbb{R}$ is the signed perpendicular distance between the plane and the origin of the reference frame. Moreover, given an arbitrary point \mathbf{p}_π in the plane, the signed perpendicular distance is given by $d_\pi = \langle \mathbf{p}_\pi, \mathbf{n}_\pi \rangle$, as illustrated in Fig. 4.

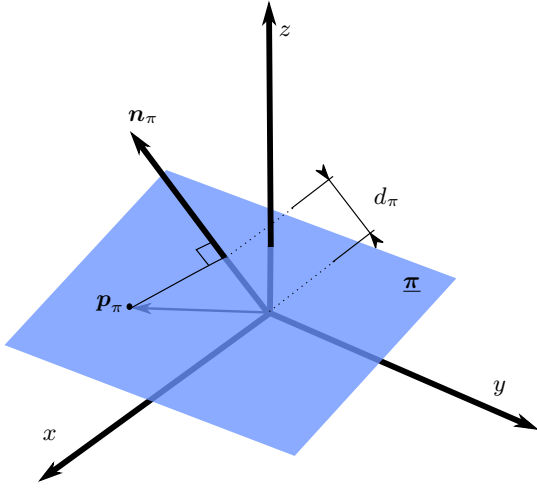


Fig. 4. Representation of a plane $\underline{\pi} \triangleq \mathbf{n}_\pi + \varepsilon d_\pi$ in dual quaternion space. The pure quaternion \mathbf{n}_π is the normal to the plane and $d_\pi = \langle \mathbf{p}_\pi, \mathbf{n}_\pi \rangle$ is the (signed) distance between the plane and the origin of the reference frame, where \mathbf{p}_π is an arbitrary point in the plane.

Consider a frame in the robot kinematic chain with pose given by $\mathbf{x} = (\mathbf{r} + \varepsilon(1/2) \mathbf{t}\mathbf{r}) \in \mathcal{S}$ and a plane $\underline{\pi}_z$, which passes through the origin of that frame, whose normal is in the same direction of the frame z -axis. Since \mathbf{x} changes according to the robot configuration—i.e., $\mathbf{x} \triangleq \mathbf{x}(\mathbf{q}(t))$ —, the plane also depends on the robot configuration; that is,

$$\underline{\pi}_z \triangleq \underline{\pi}_z(\mathbf{q}(t)) = \mathbf{n}_{\pi_z} + \varepsilon d_{\pi_z}, \quad (52)$$

where $\mathbf{n}_{\pi_z} = \mathbf{r}\hat{k}\mathbf{r}^*$ and $d_{\pi_z} = \langle \mathbf{t}, \mathbf{n}_{\pi_z} \rangle$. Since $\dot{d}_{\pi_z} = \langle \dot{\mathbf{t}}, \mathbf{n}_{\pi_z} \rangle + \langle \mathbf{t}, \dot{\mathbf{n}}_{\pi_z} \rangle$, we use (2), (6) and (26) to obtain

$$\dot{d}_{\pi_z} = \underbrace{(\text{vec}_4(\mathbf{n}_{\pi_z})^T \mathbf{J}_t + \text{vec}_4(\mathbf{t})^T \mathbf{J}_{r_z})}_{\mathbf{J}_{d_{\pi_z}}} \dot{\mathbf{q}}. \quad (53)$$

Furthermore, as the signed distance between an arbitrary point $\mathbf{p} \in \mathbb{H}_p$ in space and the plane $\underline{\pi}_z$, from the point of view of the plane [28], is

$$d_{\pi_z, \mathbf{p}}^{\pi_z} = \langle \mathbf{p}, \mathbf{n}_{\pi_z} \rangle - d_{\pi_z}, \quad (54)$$

we use (2), (26) and (53) to obtain

$$\dot{d}_{\pi_z, \mathbf{p}}^{\pi_z} = \langle \mathbf{p}, \dot{\mathbf{n}}_{\pi_z} \rangle - \dot{d}_{\pi_z} + \overbrace{\langle \dot{\mathbf{p}}, \mathbf{n}_{\pi_z} \rangle}_{\zeta_{\pi_z, \mathbf{p}}} \quad (55)$$

$$= \underbrace{(\text{vec}_4(\mathbf{p})^T \mathbf{J}_{r_z} - \mathbf{J}_{d_{\pi_z}})}_{\mathbf{J}_{\pi_z, \mathbf{p}}} \dot{\mathbf{q}} + \zeta_{\pi_z, \mathbf{p}}. \quad (56)$$

G. Robot point-to-plane distance $d_{\mathbf{t}, \pi}^{\pi}$ and Jacobian $\mathbf{J}_{\mathbf{t}, \pi}$

If \mathcal{F}_π is a frame attached to an arbitrary plane in space, the signed distance between a point $\mathbf{t} \triangleq \mathbf{t}(\mathbf{q}(t)) \in \mathbb{H}_p$ in the robot and the plane $\underline{\pi}$, from the point of view of the plane, is given by

$$d_{\mathbf{t}, \pi}^{\pi} = \langle \mathbf{t}, \mathbf{n}_\pi \rangle - d_\pi. \quad (57)$$

Using (2) and (6), the time derivative of (57) is

$$\begin{aligned} \dot{d}_{\mathbf{t}, \pi}^{\pi} &= \langle \dot{\mathbf{t}}, \mathbf{n}_\pi \rangle + \overbrace{\langle \mathbf{t}, \dot{\mathbf{n}}_\pi \rangle}_{\zeta_\pi} - \dot{d}_\pi \\ &= \underbrace{\text{vec}_4(\mathbf{n}_\pi)^T \mathbf{J}_t}_{\mathbf{J}_{\mathbf{t}, \pi}} \dot{\mathbf{q}} + \zeta_\pi \end{aligned} \quad (58)$$

$$(59)$$

V. SIMULATIONS AND EXPERIMENTS

This section presents simulations and experiments using two robotic manipulators (VS050, DENSO Corporation, Japan), each one with six degrees of freedom and equipped with a rigid 3.0 mm diameter tool. The physical robotic setup, shown in Fig. 8, is the realization of our initial concept to deal with minimally invasive transnasal microsurgery [2].

We first present simulation results to evaluate the behavior of the proposed technique under different conditions and parameters. In addition, to elucidate real-world feasibility we present two experiments with the physical robotic system: the first one is used to evaluate the effect of the parameter η_d in the vector field inequality (16); the second one is used to evaluate the use of several simultaneous active constraints to avoid collisions with an anatomically correct head model while a pair of robots automatically track a prescribed trajectory.

Both simulations and experiments used the same software implementation in a single computer running Ubuntu 16.04 x64 with a RT_PREEMPT kernel for real time control. The communication with the robots was done by using the b-Cap⁸ protocol over UDP with sampling time of 8 ms.⁹ ROS Kinetic Kame¹⁰ was used for interprocess communication of non real-time events, namely the communication with VREP and data-logging. Furthermore, dual quaternion algebra and robot kinematics were implemented using DQ Robotics¹¹ in C++, constrained convex optimization was implemented using IBM ILOG CPLEX Optimization Studio¹² with Concert Technology, and VREP [40] was used for visualization only.

In the experiments, the tool tip position with respect to the robot end effector was calibrated, by using a visual tracking system (Polaris Spectra, NDI, Canada), through a pivoting process.¹³ The visual tracking system was also used to calibrate one robot base with respect to the other.

A. Simulation A: shaft-shaft active constraint

In the first simulation two robots (R1 and R2) were positioned in opposing sides of the workspace. The robots were initially positioned so that their tool-shafts cross when viewed from the xz -plane. Both robots were commanded to simultaneously move their tools in the y -axis. The tools first moved in the same trajectory in the negative y -axis direction

⁸densorobotics.com/products/b-cap

⁹Each DENSO VS050 robot controller server runs at 125 Hz as per factory default settings.

¹⁰<http://wiki.ros.org/kinetic/Installation/Ubuntu>

¹¹<http://dqrobotics.sourceforge.net>

¹²<https://www.ibm.com/bs-en/marketplace/ibm-ilog-cplex>

¹³The pivoting process consists in adding a marker to the tool, then pivoting the tool tip about a divot and recording the marker coordinates to obtain the relative translation between marker and tool tip. This process is available in the manufacturer's software.

TABLE III
PERFORMANCE METRICS FOR SIMULATION A WITH $\eta_d = 2$.

R1	R2	$\int \ \tilde{\mathbf{x}}_1\ _2$	$\int \ \tilde{\mathbf{x}}_2\ _2$	$\int \ \tilde{\mathbf{x}}_1\ _2 + \int \ \tilde{\mathbf{x}}_2\ _2$	collision
o	o	0.1484	0.1488	0.2973	yes
o	s	0.14845	8.1995	8.3479	yes
s	o	7.93310	0.1488	8.0819	yes
o	k	0.1484†	6.1087*	6.2571	no
s	s	3.22129	5.7271	8.9483*	no
s	k	4.2704	3.2258	7.4962	no
k	o	6.1498*	0.1488†	6.2986	no
k	s	1.97851	5.9864	7.9649	no
k	k	3.0947	3.1159	6.2107†	no

Robots R1 and R2 can be oblivious (*o*), static aware (*s*), and kinematics aware (*k*). Moreover, $\tilde{\mathbf{x}}_1$ is the trajectory error of R1, and $\tilde{\mathbf{x}}_2$ of R2. Lastly, we considered a collision whenever the distance between shafts was smaller than 3 mm. Considering only cases with no collision, values with † are the best values in each column and values with * are the worst values in each column.

such that R1 followed R2 with a slight offset during $t \in [0, 2s)$, then both robots kept the simultaneous motion but changed the direction along the y -axis so that R2 followed R1 during $t \in [2s, 4s)$, then moved toward each other during $t \in [4s, 6s)$, and finally moved away from each other during $t \in [6s, 8s]$. The reference trajectory required the tool orientations to remain constant.

In order to study the dynamic active constraint to prevent collision between shafts, we consider three different ways of generating the control inputs. In the first one, the control input is generated by the solution of Problem (8); therefore, as the robot does not take into account any obstacle and is unaware of its surroundings, we say it is *oblivious*. In the second and third ones, the control input is generated by the solution of Problem (10) with Constraint 18 and (48), (49), and (50). However, in the second one the residual is not used, thus the robot is *static aware*; that is, the robot considers its surroundings, but does not take into account obstacle kinematics. In the third one, a robot controlled with the full proposed dynamic active constraints, including the residual, is called *kinematics aware* robot. If both robots are kinematics aware, the centralized Problem (12) was used to solve for both robots simultaneously. With these definitions, we examine every unique combination of states between robots for convergence rate $\eta = 50$, approach gain $\eta_d \in \{0, 1, 2, 3, 4, 5, 6, 7, 8.5, 10\}$, and sampling time $\tau = 8$ ms.

The design parameter η_d corresponds to the fastest distance decay allowed between two moving robotic systems; therefore, in a system where both robots are kinematically aware, have the same approach gain η_d , and move directly towards each other, the result of the optimization will assign a gain $\eta_d/2$ for each robot in the most restrictive case. Thus, to provide a fair comparison in the same scenario, when both robots are static aware the approach gain (η_d) was divided in half.

1) *Results and discussion*: The performance for $\eta_d = 2$ in terms of trajectory tracking error and minimum separating distance is summarized in Table III. The continuous behavior can be seen in Fig. 5. Since simulations for other approach gains show a similar trend, they are omitted.

When both robots were oblivious, the tool shafts collided as no constraints were enabled. When one robot was static

aware and the other robot was oblivious, a snapshot vision of the world was not enough to avoid collisions. In the remaining cases, collisions were effectively avoided.

When both R1 and R2 were static aware robots, the sum of the tracking errors for R1 and R2 was the largest. As the robots considered each other as an instantaneously static obstacle, they slowed down to avoid collisions, even when other robot was effectively moving away. This behavior is shown in Fig. 5 for R1 between 0 and 2 seconds, and for R2 between 2 and 4 seconds. These results indicate that tracking error is suboptimal when using only static awareness, even though such configuration might be reliable to prevent collisions if both arms implement it. For instance, if one of the tools is directly manipulated by a surgeon, it may be hard to estimate their tool's velocity, but as shown by our results, only the tool's position is needed to prevent collisions since the surgeon will use their static knowledge to avoid dangerous interactions between tools.

When one robot was kinematics aware and the other was oblivious, the oblivious robot followed its trajectory with minimum error, as it was unaware of the existence of the other robot. The kinematics aware robot used the kinematics knowledge to fully undertake evasive maneuvers. Such results indicate that this configuration may be useful in practical scenarios in which one robot has a clear priority over the other. For instance, this configuration would be useful when a human collaborator handles a sensorized tool from which velocity and position can be extracted.

When both robots were kinematics aware, they had the best combined trajectory tracking for cases in which no collision happened. Indeed, this happened because such configuration provides a more suitable problem description, which is to minimize the sum of the trajectory errors under the anti-collision constraints. In fact, adding the residual information in Problem 12 allows the system to optimize the approach velocity when one entity is moving away. Such behavior justifies the implementation of dynamic active constraints whenever feasible.

B. Experiment A: plane active constraint

In this experiment we evaluated the behavior of the robot when its tool tip was commanded to reach a location beyond a static plane boundary, while studying different approach gains for the point-to-plane active constraint. The experimental setup is shown in Fig. 6.

The initial robot configuration was $\mathbf{q}(0) = [\pi/6 \ \pi/2 \ 0 \ 0 \ -\pi/6 \ 0]^T$ rad, and the robot was commanded to move down 45 mm in the world z -axis, while the rotation was fixed with the tool tip pointing downward. The constraint consisted of a static plane orthogonal to the z -axis and positioned 25 mm below the initial tool tip position. Hence, a collision was expected after the tool tip moved 25 mm downwards. Initial condition and reference trajectory were the same for all executions.

In the first execution, there was no plane constraint. To study the effects of different active constraint gains, we chose gains in the set $\eta_\pi = \{0, 0.25, 1, 4, 16\}$ in each execution.

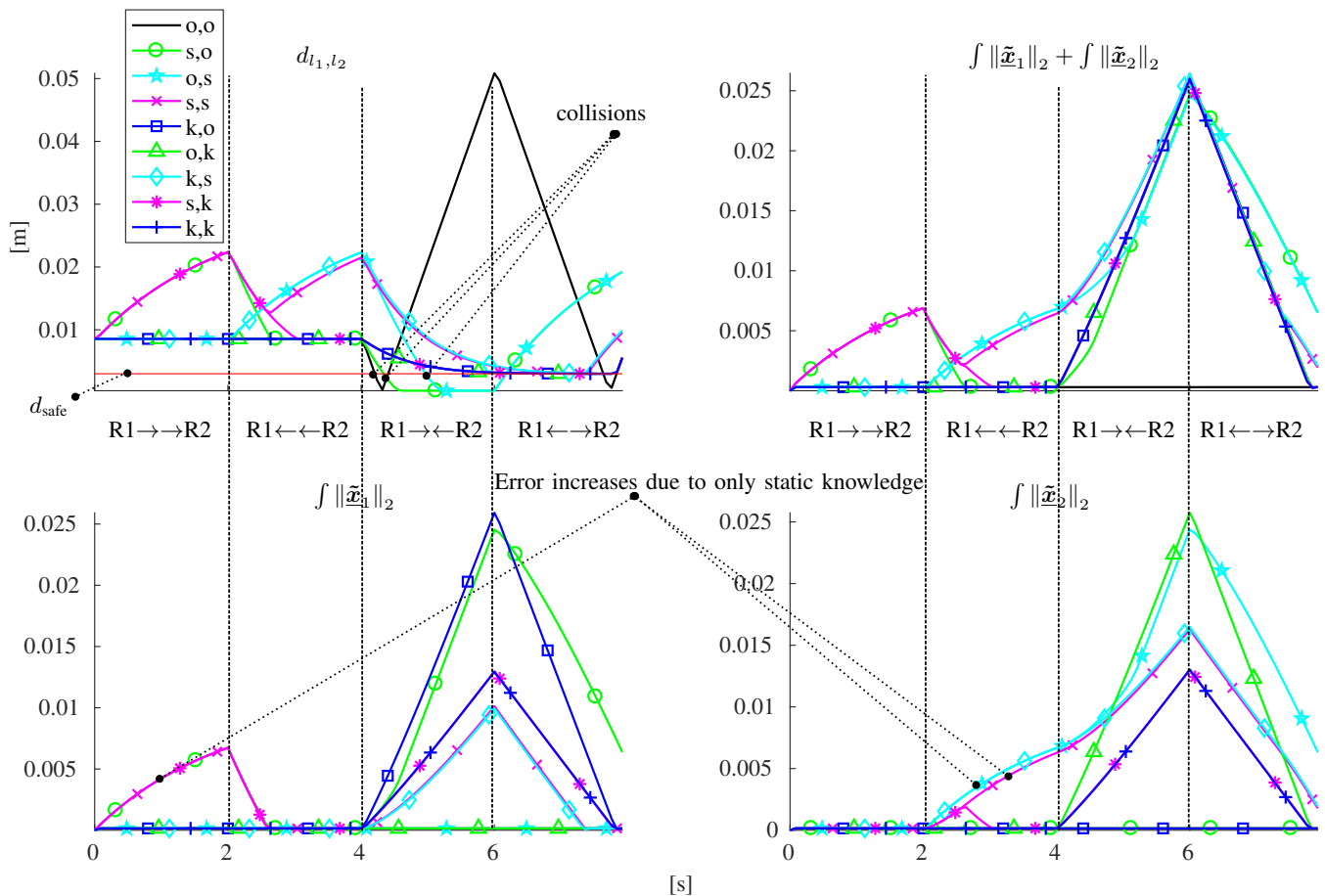


Fig. 5. Simulation A. The vertical dashed bars represent the transition to a different phase, which are named as: $R1 \rightarrow R2$ when $R1$ moved in the direction of $R2$, which moved away; $R1 \leftarrow R2$ when $R2$ moved in the direction of $R1$, which moved away; $R1 \rightarrow R2$ when the robots moved towards each other; and $R1 \leftarrow R2$ when the robots moved away from each other. Collisions only happened in the set $\{\{o, o\}, \{o, s\}, \{s, o\}\}$.

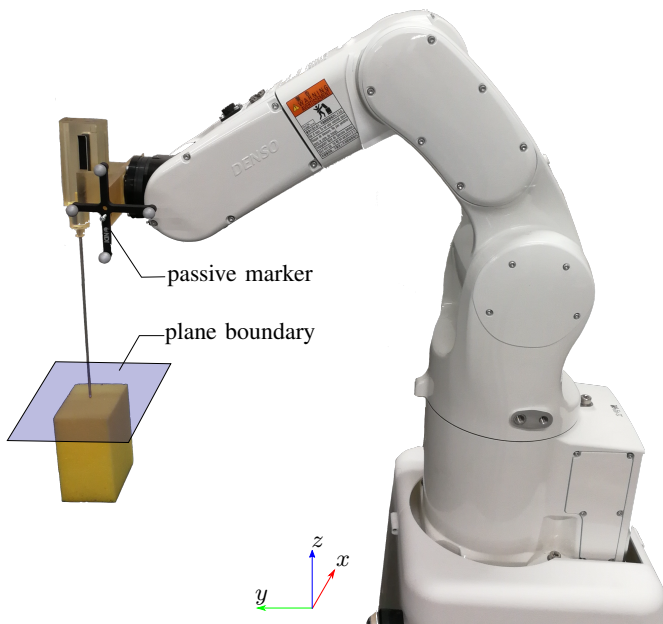


Fig. 6. Setup for experiment A, described in Section V-B. A single robot was used and the passive marker was used to calibrate the tool tip. The plane was chosen so that the tool tip did not touch the yellow sponge cube.

1) *Results and discussion:* As shown in Fig. 7, when the active constraint was not activated, the end effector moved through the plane and the trajectory had minimum tracking error, as nothing constrained the motion.

When $\eta_\pi = 0$, the end effector was not allowed to approach the plane. As the vector field inequality gain increased, the end effector was allowed to approach faster, as shown by the exponential behavior in Fig. 7. Even with an increase in tracking error norm, as shown in the bottom graph in Fig. 7, the end effector did not cross the plane with any value for the approach gain, which is predicted by the theory, and there was no sudden activation of the joints as would happen if position-based constrained optimization [10], [11] was used.

For this experiment (i.e., six executions, each one corresponding to one approach gain), the full control loop had an average computation time of 3.9 ms with standard deviation of 0.6804 ms in non-optimized C++ code.

C. Experiment B: constrained workspace manipulation

This section presents experiments in a mockup of a constrained neurosurgical setup, shown in Fig. 8, for dura mater

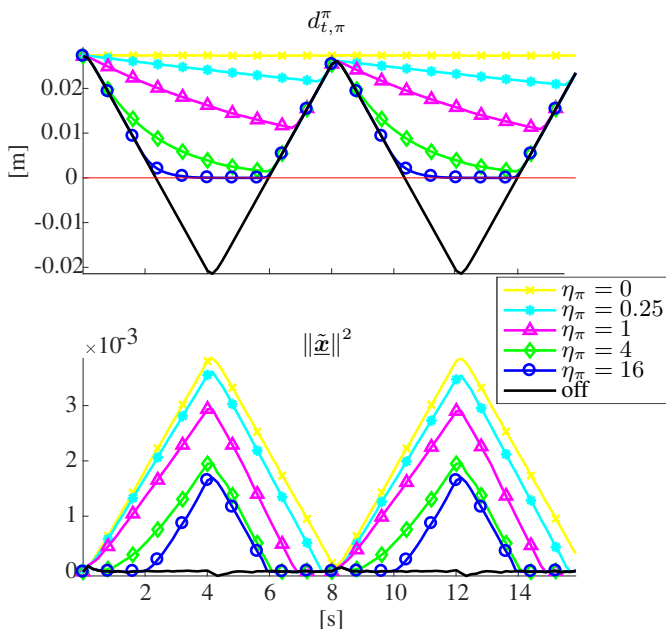


Fig. 7. Results of six executions in Experiment A, where a static plane generated a forbidden region, as described in Section V-B. The distance between the end effector and the plane is shown on *top* and the 2-norm of the pose error, as the robot tracked the desired trajectory, is shown on the *bottom* graph. The distance limit is represented by the red line, and whenever the active constraint was enabled the end effector did not go through the plane.

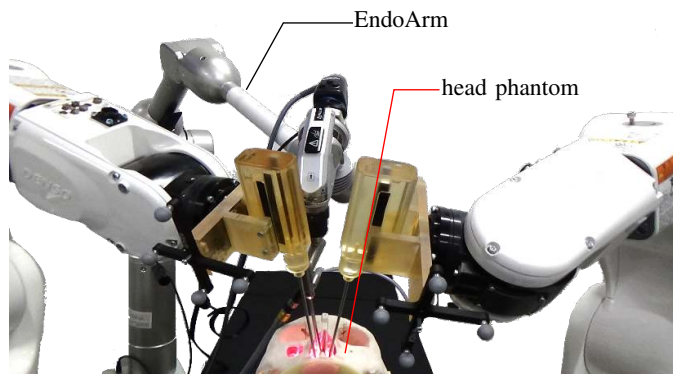


Fig. 8. Setup for the experiment described in section V-C.

manipulation.¹⁴

The mockup consisted of a pair of manipulators positioned at each side of a 3D printed head model, which was based on human anatomy and developed in a cooperation between the National Institute of Advanced Industrial Science and Technology (AIST) and the Meijo University. The head model was customized to our needs by adding the target dura mater. For high-definition vision, we used a 30° endoscope (Olympus, Japan) attached to a manually operated endoscope

¹⁴In pituitary gland resection, long thin tools are inserted through the nasal cavity to reach the sphenoid sinus. To increase workspace in the nasal cavity, some turbinates (i.e., protruding bones in the nasal cavity with several physiological uses, which can be removed to some extent without major impact on the patient's health) are removed by an ear, nose, and throat (ENT) specialist. After the clean-up done by the ENT specialist, a neurosurgeon takes place and removes a thin bone shell protecting the sphenoid sinus, exposing the dura mater. After being exposed, the dura mater is cut, the pituitary gland is resected, and the dura mater is then sutured.

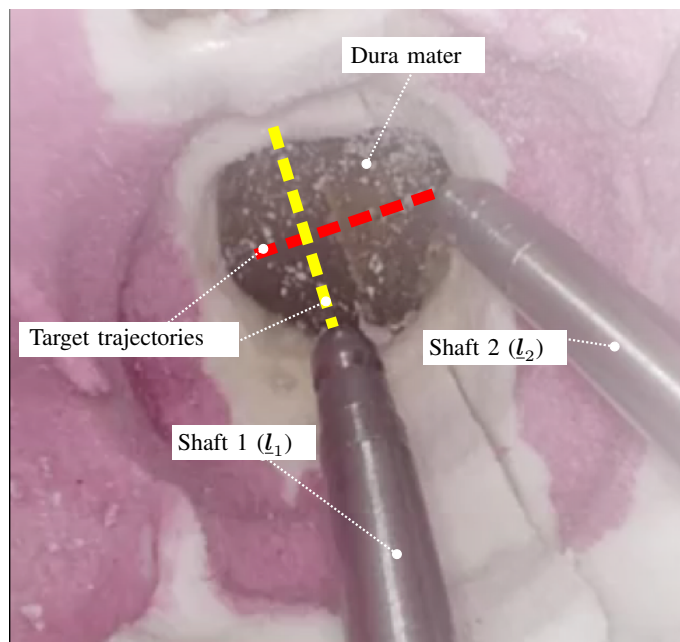


Fig. 9. Setup for the experiment described in Section V-C.

holder (EndoArm, Olympus, Japan). The dura mater and the surgical tool tips, along with the desired trajectories, are shown in Fig. 9. As we used a mock tool without any actuation, the whole system had 6 DOF for each robotic manipulator. Furthermore, only the tool tip trajectory was controlled, hence the robot was redundant to the task, having a surplus of 3 DOF.

Although this experiment was devised to be as close as possible to a clinical scenario, it does not aim to be by itself clinically relevant as it would require several considerations outside the scope of this paper. Therefore, the purpose of this experiment is to evaluate if the proposed active constraints can be used in a realistic environment, and to answer the following research questions:

- 1) Do the added disturbances of physical robotic systems destabilize the control law?
- 2) Can a complex environment be effectively modeled by using the proposed primitives?
- 3) Is there a feasible method to calibrate the robotic systems to obtain reasonable accuracy?

These questions define whether collisions can be effectively prevented by using kinematic information of both robots and workspace.

Three groups of active constraints were used. The first group was composed of robot line-to-point constraints (see Fig. 10). A pair of points were placed in the entrance of the nostrils with positions \mathbf{p}_{nl} and \mathbf{p}_{nr} , another pair in the end of the sinus \mathbf{p}_{el} and \mathbf{p}_{er} , and a last point positioned at the center of the dura mater, \mathbf{p}_m . Moreover, the left robot's tool shaft was collinear with the Plücker line $\mathbf{l}_1 \triangleq \mathbf{l}_1(\mathbf{q}_1)$ and the right robot's tool shaft was collinear with $\mathbf{l}_2 \triangleq \mathbf{l}_2(\mathbf{q}_2)$. The distance between shafts and points were constrained to specify safe zones for tools in order to prevent collisions between tool shafts and the head model. This way, the first group of constraints related to

the first robot were chosen as

$$\begin{aligned} \mathcal{C}_{l_1, p_{nl}}^1 &\triangleq \mathbf{J}_{l_1, p_{nl}} \dot{\mathbf{q}}_1 \leq \eta_{l_1, p_{nl}} \tilde{D}_{l_1, p_{nl}}, \\ \mathcal{C}_{l_1, p_{el}}^2 &\triangleq \mathbf{J}_{l_1, p_{el}} \dot{\mathbf{q}}_1 \leq \eta_{l_1, p_{el}} \tilde{D}_{l_1, p_{el}}, \\ \mathcal{C}_{l_1, p_m}^3 &\triangleq \mathbf{J}_{l_1, p_m} \dot{\mathbf{q}}_1 \leq \eta_{l_1, p_m} \tilde{D}_{l_1, p_m}, \end{aligned}$$

and the ones related to the second robot were chosen as

$$\begin{aligned} \mathcal{C}_{l_2, p_{nr}}^4 &\triangleq \mathbf{J}_{l_2, p_{nr}} \dot{\mathbf{q}}_2 \leq \eta_{l_2, p_{nr}} \tilde{D}_{l_2, p_{nr}}, \\ \mathcal{C}_{l_2, p_{er}}^5 &\triangleq \mathbf{J}_{l_2, p_{er}} \dot{\mathbf{q}}_2 \leq \eta_{l_2, p_{er}} \tilde{D}_{l_2, p_{er}}, \\ \mathcal{C}_{l_2, p_m}^6 &\triangleq \mathbf{J}_{l_2, p_m} \dot{\mathbf{q}}_2 \leq \eta_{l_2, p_m} \tilde{D}_{l_2, p_m}, \end{aligned}$$

where both squared distance functions and Jacobians were chosen as in (33) and (34), respectively. Since the points attached to the head model did not change during the whole experiments, the corresponding residuals are zero.

The second group of constraints was composed of four robot plane-to-point constraints, as illustrated in Fig. 11. The plane attached to the left robot is given by $\pi_1 \triangleq \pi_1(\mathbf{q}_1)$ and the points attached to the right robot are given by $p_{R2,i} \triangleq p_{R2,i}(\mathbf{q}_2)$, $i \in \{1, 2, 3, 4\}$. In order to constrain the distance between those points and the plane (thus preventing collision between the tool modules outside the patient), the four constraints of the second group were chosen as

$$\mathcal{C}_{R2,i}^{i+6} \triangleq -\mathbf{J}_{\pi_1, R2,i} \dot{\mathbf{q}}_1 - \mathbf{J}_{R2,i, \pi_1} \dot{\mathbf{q}}_2 \leq \eta_{\pi_1, R2,i} \tilde{D}_{\pi_1, R2,i}.$$

Lastly, a combination of robot line-to-point and robot line-to-line constraints were used to prevent collisions between the shafts, each modeled as a line with the tool tip as one endpoint. Let the tool tip positions be given by $t_1 \triangleq t_1(\mathbf{q}_1)$ and $t_2 \triangleq t_2(\mathbf{q}_2)$. Each semi-infinite cylinder was therefore $c_1 \triangleq c_1(t_1, \underline{l}_1, d_{\text{safe1}})$ and $c_2 \triangleq c_2(t_2, \underline{l}_2, d_{\text{safe2}})$, in which d_{safe1} and d_{safe2} represent their radiuses. This was implemented as two constraints:

$$\mathcal{C}_{c_1, c_2}^{11} \triangleq \begin{cases} -\mathbf{J}_{t_1, l_2} \dot{\mathbf{q}}_1 - \mathbf{J}_{l_2, t_1} \dot{\mathbf{q}}_2 \leq \eta_{t_1, l_2} \tilde{D}_{t_1, l_2} & \text{if } \text{proj}_{l_2}(t_1) \in c_2, \\ -\mathbf{J}_{t_2, l_1} \dot{\mathbf{q}}_2 - \mathbf{J}_{l_1, t_2} \dot{\mathbf{q}}_1 \leq \eta_{t_2, l_1} \tilde{D}_{t_2, l_1} & \text{if } \text{proj}_{l_1}(t_2) \in c_1, \\ \mathbf{0}^T \dot{\mathbf{q}}_1 + \mathbf{0}^T \dot{\mathbf{q}}_2 \leq 0 & \text{otherwise,} \end{cases}$$

in which $\text{proj}_{\underline{l}}(\mathbf{p})$ is the projection of \mathbf{p} onto \underline{l} and

$$\mathcal{C}_{c_1, c_2}^{12} \triangleq \begin{cases} -\mathbf{J}_{l_1, l_2} \dot{\mathbf{q}}_1 - \mathbf{J}_{l_2, l_1} \dot{\mathbf{q}}_2 \leq \eta_{l_1, l_2} \tilde{D}_{l_1, l_2} & \text{if } \text{proj}_{l_1}(l_2) \in c_2 \\ & \text{and } \text{proj}_{l_2}(l_1) \in c_1, \\ \mathbf{0}^T \dot{\mathbf{q}}_1 + \mathbf{0}^T \dot{\mathbf{q}}_2 \leq 0 & \text{otherwise.} \end{cases}$$

Arbitrary collisions between cylinders is the topic of extensive research [41], [42] and we focused only on relevant collisions for this experiment.

In total, twelve constraints were used in the control algorithm, whose control input was generated by the solution of Problem 12. Similar to real surgery, the endoscope was positioned in such a way as to not disturb the tool motion, therefore no specific active constraints were required for the endoscope.

The experiment was divided into three parts, all with the same initial configuration, as shown in Fig. 9. The trajectories consisted of a straight line connecting the start and end points, which were automatically tracked by the tool tips. The first

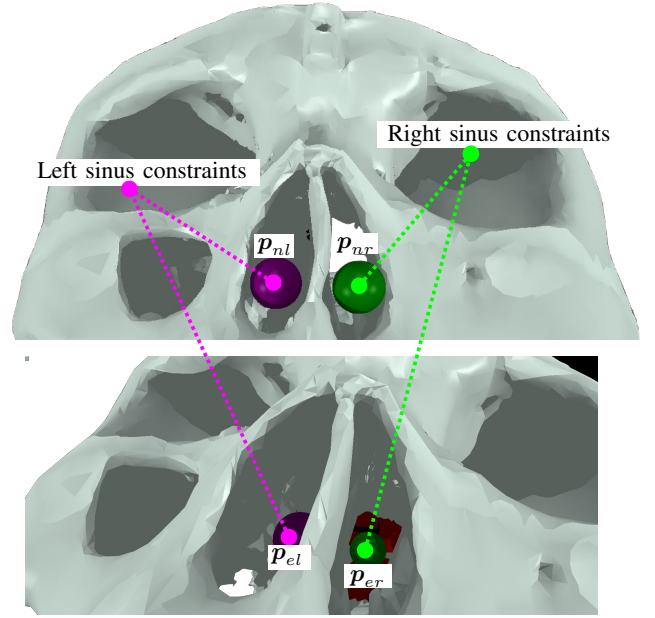


Fig. 10. 3D computer model of the compliant pivoting points used to prevent collisions between the tool shafts and the anatomical model. The points were fixed with respect to the head model, and the distance between points and tool shafts was actively constrained.

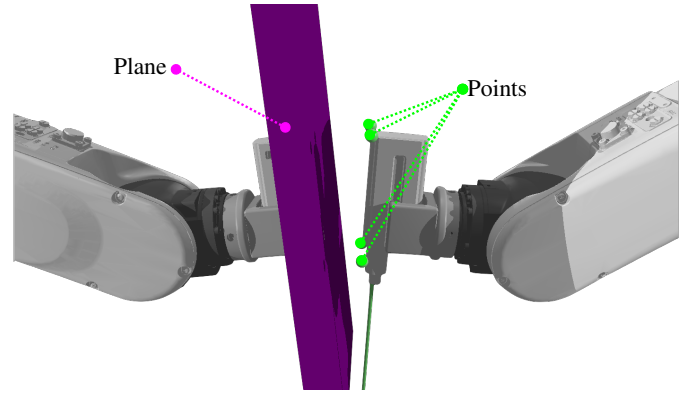


Fig. 11. 3D computer model of the constraints used to prevent collisions between the forceps modules. A dynamic plane was rigidly attached to the left robot whereas four points were rigidly attached to the right robot. The distance between the plane and the points was actively constrained.

part consisted of letting the right tool static and moving the left tool from the initial bottom position to the top, along the yellow trajectory, and returning. The second part consisted of letting the left tool static while moving the right tool, from the initial right position along the red trajectory to its leftmost point, and returning. The last part consisted of moving both tools simultaneously along their predefined trajectories. The same set of constraints were used in all three parts. The two first parts were used as ground-truth, as collisions were not expected between tools. The last part required the tools to follow a trajectory that would cause a collision unless the manipulators performed evasive maneuvers.

The control parameters related to the objective function were $\eta = 300$ and $\lambda = 0.1$. All constraints used the same approach gain $\eta_d = 2$.

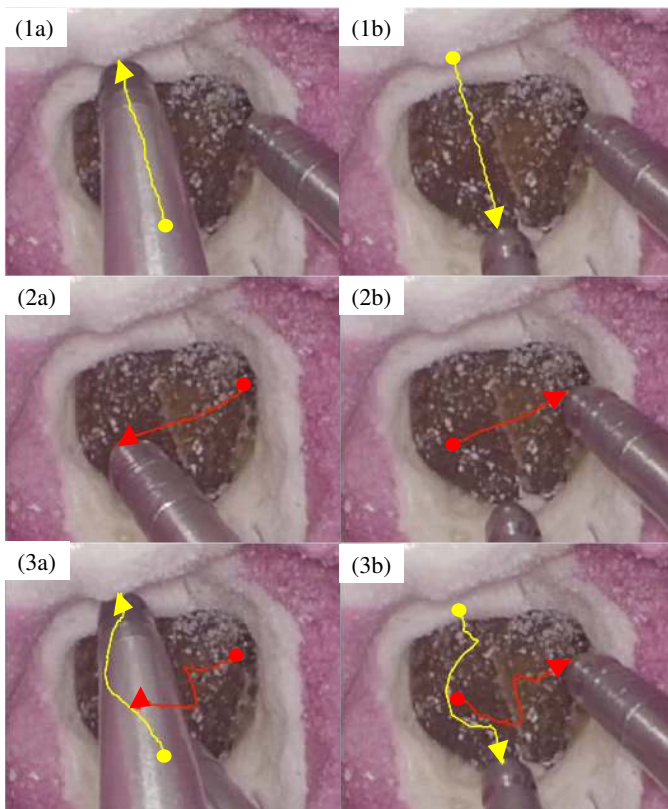


Fig. 12. Tracking results for the three experimental runs described in Section V-C. Each trajectory was divided into two parts for clarity, and the executed trajectory in each case was obtained by manually marking tool tip pixels every ten video frames. In each trajectory, a circle marks its beginning and an arrowhead marks its end. Figures 1a and 1b show the trajectories executed by the left tool while the right tool was fixed. Conversely, Figs. 2a and 2b show the trajectories executed by the right tool while the left tool was fixed. Lastly, Figs. 3a and 3b show the trajectories executed when both tools moved simultaneously, illustrating how, in order to avoid collisions, both tools deviated from the prescribed trajectory.

1) *Results and discussion:* A representative trajectory for each of the three runs is shown in Fig. 12. As the manipulator robots have rigid links and had high-accuracy calibration, all executions effectively yielded the same results. A sequence of snapshots is shown in Fig. 12, showing how the collision avoidance was performed.

Fig. 13 shows the signed distances between the actively constrained elements, which were calculated using the robots' kinematic models. A negative signed distance means that a collision happened. Possible collisions with the head model were visually inspected.

As shown in Fig. 12, when only one tool moved, the desired trajectory was tracked without major deviations. Using that effective trajectory as comparison point, Fig. 12 also shows the required deviation when both tools moved simultaneously so that no collision would happen.

The distance measurements done using the robots' kinematics, as shown in Fig. 13, show that the disturbances and noise caused by the experimental system did not affect the usability of the proposed framework. This experimentally validates the results initially studied in Section V-A.

Decomposing the workspace into primitives provided safety

without hindering tool motion. In contrast with techniques that require full knowledge of the anatomy [11], [24], the proposed methodology can be used intraoperatively and is computationally efficient. For instance, the surgeon can define regions inside the workspace in succession to define where the compliant pivoting points should be located and build the safe regions for the tools.

A major point of concern is the level of accuracy of the calibration, since it directly affects kinematic control laws such as the one proposed in this work. In these experiments, which were sufficiently complex, a relatively common visual tracking system was enough to provide a reasonable level of accuracy, but some inaccuracy was still visible. The inaccuracy caused by the system can be qualitatively seen when comparing the expected simulated motion and the actual robot motion. The major source of discrepancies in this case was the calibration of the tool shaft axes, which was not directly done. This is a topic of ongoing research in our group.

This experiment showed the capabilities of the proposed framework in a constrained workspace. Future works will be focused on taking these results into a more clinical setup. When robots are teleoperated, the surgeon's judgment is necessary to decide which collisions should be avoided and how much autonomy the robotic system can have. For instance, with an actuated tool, the operator may wish that translation is prioritized over rotation. Moreover, in a given scenario, they might want tools to halt instead of autonomously avoiding collisions between each other. Lastly, in this experiment both tools shared the burden of avoiding collisions. In some procedures, however, it may be more intuitive for the operator if the system prioritizes one tool over the other.

VI. CONCLUSIONS

This paper extended our previous work [28] to consider dynamic active constraints. The method can be used to keep the robot from entering a restricted zone or to maintain the robot inside a safe area, and is based in a solution that takes into account both equality and inequality constraints. The vector field inequalities limit the velocity of the robot in the direction of the restricted zone's boundary and leaves tangential velocities undisturbed. The method requires a Jacobian that describes the relation between the time derivative of the distance and robot joints' velocities, as well as a residual that encodes the kinematics information for dynamic objects. We derive Jacobians and residuals for relations in which both entities can be dynamic; namely, point-point, point-line, line-line, and point-plane. In simulated experiments, a pair of six-DOF robot manipulators equipped with endonasal tool mockups was used to evaluate the behavior of the proposed technique under different conditions and parameters. The results have shown that by using the vector field inequalities for dynamic objects, the combined trajectory error of two robotic systems is optimal. After, experiments using the real robotic system have shown that the method can be applied in physical systems to autonomously prevent collisions between the moving robots themselves and between the robots and the environment.

The proposed method have shown good results with a reasonably simple calibration procedure using passive markers

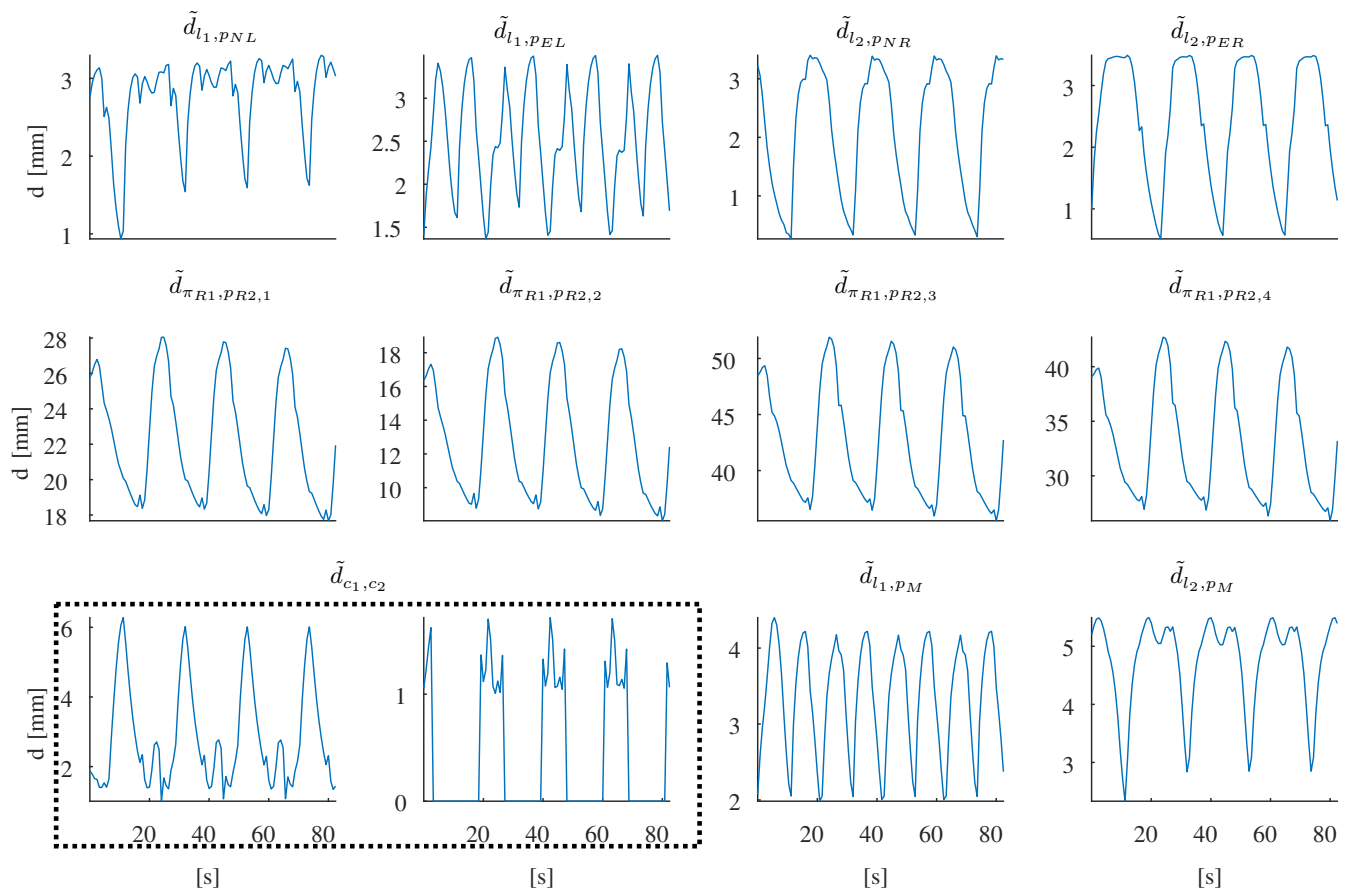


Fig. 13. Signed distances between primitives in the third part of Experiment B, in which both robots moved. Four sequential repetitions of the same motion are shown. In each plot, positive signed distance means that the robot is in the safe zone; as a negative value would mean that the constraint was violated, all curves show that the constraints were respected throughout the whole experiment.



Fig. 14. Snapshots of the tool evasion in the third automatic tracing experiment, in which both robots moved. The left tool uses the dynamic knowledge of the right tool to initiate the evasive maneuvers before getting close to it.

and a visual tracking system. A current line of research is focused on the integration of dynamic active constraints with tracking algorithms that use the endoscopic images, which may increase overall accuracy of the method. Moreover, clinically-oriented studies regarding the teleoperation of the robotic system with a novel four-DOF tool are currently in progress.

REFERENCES

- [1] H. Ueda, R. Suzuki, A. Nakazawa, Y. Kurose, M. M. Marinho, N. Shono, H. Nakatomi, N. Saito, E. Watanabe, A. Morita, K. Harada, N. Sugita, and M. Mitsuishi, "Toward autonomous collision avoidance for robotic neurosurgery in deep and narrow spaces in the brain," *Procedia CIRP*, vol. 65, no. Supplement C, pp. 110 – 114, 2017. 3rd CIRP Conference on BioManufacturing.
- [2] M. Marinho, A. Nakazawa, J. Nakanishi, T. Ueyama, Y. Hasegawa, J. Arata, M. Mitsuishi, and K. Harada, "Conceptual design of a versatile robot for minimally invasive transnasal microsurgery," in *MicroMechatronics and Human Science (MHS), 2016 International Symposium on*, pp. 1–3, IEEE, 2016.
- [3] A. Morita, S. Sora, M. Mitsuishi, S. Warisawa, K. Suruman, D. Asai, J. Arata, S. Baba, H. Takahashi, R. Mochizuki, *et al.*, "Microsurgical robotic system for the deep surgical field: development of a prototype and feasibility studies in animal and cadaveric models," *Journal of neurosurgery*, vol. 103, no. 2, pp. 320–327, 2005.
- [4] Y. Ida, N. Sugita, T. Ueta, Y. Tamaki, K. Tanimoto, and M. Mitsuishi, "Microsurgical robotic system for vitreoretinal surgery," *International journal of computer assisted radiology and surgery*, vol. 7, no. 1, pp. 27–34, 2012.
- [5] M. Mitsuishi, A. Morita, N. Sugita, S. Sora, R. Mochizuki, K. Tanimoto, Y. M. Baek, H. Takahashi, and K. Harada, "Master-slave robotic platform and its feasibility study for micro-neurosurgery," *The International Journal of Medical Robotics and Computer Assisted Surgery*, vol. 9, no. 2, pp. 180–189, 2013.
- [6] A. Nakazawa, K. Nanri, K. Harada, S. Tanaka, H. Nukariya, Y. Kurose, N. Shono, H. Nakatomi, A. Morita, E. Watanabe, *et al.*, "Feedback methods for collision avoidance using virtual fixtures for robotic neurosurgery in deep and narrow spaces," in *Biomedical Robotics and*

- Biomechatronics (BioRob)*, 2016 6th IEEE International Conference on, pp. 247–252, IEEE, 2016.
- [7] R. Taylor, P. Jensen, L. Whitcomb, A. Barnes, R. Kumar, D. Stoianovici, P. Gupta, Z. Wang, E. Dejuan, and L. Kavoussi, “A steady-hand robotic system for microsurgical augmentation,” *The International Journal of Robotics Research*, vol. 18, no. 12, pp. 1201–1210, 1999.
- [8] J. G. Petersen, S. A. Bowyer, and F. R. y Baena, “Mass and friction optimization for natural motion in hands-on robotic surgery,” *IEEE Transactions on Robotics*, vol. 32, no. 1, pp. 201–213, 2016.
- [9] B. Siciliano, L. Sciacivco, L. Villani, and G. Oriolo, *Robotics: Modelling, Planning and Control*. Advanced Textbooks in Control and Signal Processing, London: Springer-Verlag London, 2009.
- [10] A. Kapoor, M. Li, and R. H. Taylor, “Constrained control for surgical assistant robots,” in *Robotics and Automation (ICRA)*, 2006 IEEE International Conference on, pp. 231–236, 2006.
- [11] M. Li, M. Ishii, and R. H. Taylor, “Spatial motion constraints using virtual fixtures generated by anatomy,” *IEEE Transactions on Robotics*, vol. 23, no. 1, pp. 4–19, 2007.
- [12] S. A. Bowyer, B. L. Davies, and F. R. y Baena, “Active constraints/virtual fixtures: A survey,” *IEEE Transactions on Robotics*, vol. 30, no. 1, pp. 138–157, 2014.
- [13] Z. Chen, A. Malpani, P. Chalasani, A. Deguet, S. S. Vedula, P. Kazanzides, and R. H. Taylor, “Virtual fixture assistance for needle passing and knot tying,” in *Intelligent Robots and Systems (IROS)*, 2016 IEEE/RSJ International Conference on, pp. 2343–2350, IEEE, 2016.
- [14] M.-A. Vitrani, C. Poquet, and G. Morel, “Applying virtual fixtures to the distal end of a minimally invasive surgery instrument,” *IEEE Transactions on Robotics*, vol. 33, no. 1, pp. 114–123, 2017.
- [15] T. L. Gibo, L. N. Verner, D. D. Yuh, and A. M. Okamura, “Design considerations and human-machine performance of moving virtual fixtures,” in *Robotics and Automation, 2009. ICRA’09. IEEE International Conference on*, pp. 671–676, IEEE, 2009.
- [16] K.-W. Kwok, G. P. Mylonas, L. W. Sun, M. Lerotic, J. Clark, T. Athanasiou, A. Darzi, and G.-Z. Yang, “Dynamic active constraints for hyper-redundant flexible robots,” in *International Conference on Medical Image Computing and Computer-Assisted Intervention*, pp. 410–417, Springer, 2009.
- [17] N. V. Navkar, Z. Deng, D. J. Shah, K. E. Bekris, and N. V. Tsekos, “Visual and force-feedback guidance for robot-assisted interventions in the beating heart with real-time mri,” in *Robotics and Automation (ICRA)*, 2012 IEEE International Conference on, pp. 689–694, IEEE, 2012.
- [18] F. Rydén and H. J. Chizeck, “Forbidden-region virtual fixtures from streaming point clouds: Remotely touching and protecting a beating heart,” in *Intelligent Robots and Systems (IROS)*, 2012 IEEE/RSJ International Conference on, pp. 3308–3313, IEEE, 2012.
- [19] J. Ren, R. V. Patel, K. A. McIsaac, G. Guiraudon, and T. M. Peters, “Dynamic 3-d virtual fixtures for minimally invasive beating heart procedures,” *IEEE transactions on medical imaging*, vol. 27, no. 8, pp. 1061–1070, 2008.
- [20] K.-W. Kwok, K. H. Tsoi, V. Vitiello, J. Clark, G. C. Chow, W. Luk, and G.-Z. Yang, “Dimensionality reduction in controlling articulated snake robot for endoscopy under dynamic active constraints,” *IEEE Transactions on Robotics*, vol. 29, no. 1, pp. 15–31, 2013.
- [21] K.-W. Kwok, V. Vitiello, and G.-Z. Yang, “Control of articulated snake robot under dynamic active constraints,” *Medical Image Computing and Computer-Assisted Intervention—MICCAI 2010*, pp. 229–236, 2010.
- [22] B. C. Becker, R. A. MacLachlan, L. A. Lobes, G. D. Hager, and C. N. Riviere, “Vision-based control of a handheld surgical micromanipulator with virtual fixtures,” *IEEE Transactions on Robotics*, vol. 29, no. 3, pp. 674–683, 2013.
- [23] J. Funda, R. H. Taylor, B. Eldridge, S. Gomory, and K. G. Gruben, “Constrained cartesian motion control for teleoperated surgical robots,” *IEEE Transactions on Robotics and Automation*, vol. 12, no. 3, pp. 453–465, 1996.
- [24] T. Xia, C. Baird, G. Jallo, K. Hayes, N. Nakajima, N. Hata, and P. Kazanzides, “An integrated system for planning, navigation and robotic assistance for skull base surgery,” *The International Journal of Medical Robotics and Computer Assisted Surgery*, vol. 4, no. 4, pp. 321–330, 2008.
- [25] R. Prada and S. Payandeh, “On study of design and implementation of virtual fixtures,” *Virtual reality*, vol. 13, no. 2, pp. 117–129, 2009.
- [26] B. Faverjon and P. Tournassoud, “A local based approach for path planning of manipulators with a high number of degrees of freedom,” in *Robotics and Automation. Proceedings. 1987 IEEE International Conference on*, vol. 4, pp. 1152–1159, IEEE, 1987.
- [27] O. Kanoun, F. Lamiroux, and P.-B. Wieber, “Kinematic control of redundant manipulators: Generalizing the task-priority framework to inequality task,” *IEEE Transactions on Robotics*, vol. 27, no. 4, pp. 785–792, 2011.
- [28] M. M. Marinho, B. V. Adorno, K. Harada, and M. Mitsuishi, “Active constraints using vector field inequalities for surgical robots,” in *Robotics and Automation (ICRA)*, 2018 IEEE International Conference on (Preprint available online at <http://arxiv.org/abs/1804.03883>), IEEE, 2018.
- [29] B. V. Adorno, *Two-arm Manipulation: From Manipulators to Enhanced Human-Robot Collaboration [Contribution à la manipulation à deux bras : des manipulateurs à la collaboration homme-robot]*. PhD Dissertation, Université Montpellier 2, 2011.
- [30] A. T. Yang, *Application of quaternion algebra and dual numbers to the analysis of spatial mechanisms*. PhD thesis, Columbia University., 1963.
- [31] A. Perez and J. M. McCarthy, “Dual Quaternion Synthesis of Constrained Robotic Systems,” *Journal of Mechanical Design*, vol. 126, no. 3, pp. 425–435, 2004.
- [32] J. J. Quiroz-Omaña and B. V. Adorno, “Whole-Body Kinematic Control of Nonholonomic Mobile Manipulators Using Linear Programming,” *Journal of Intelligent & Robotic Systems*, in press.
- [33] B. V. Adorno, “Robot kinematic modeling and control based on dual quaternion algebra — Part I: Fundamentals,” 2017.
- [34] J. M. Selig, *Geometric fundamentals of robotics*. Springer-Verlag New York Inc., 2nd ed., 2005.
- [35] B. V. Adorno, P. Fraisse, and S. Druon, “Dual position control strategies using the cooperative dual task-space framework,” in *Intelligent Robots and Systems (IROS)*, 2010 IEEE/RSJ International Conference on, pp. 3955–3960, IEEE, 2010.
- [36] S. Boyd and L. Vandenberghe, *Convex optimization*. Cambridge university press, 2004.
- [37] A. Escande, N. Mansard, and P.-B. Wieber, “Hierarchical quadratic programming: Fast online humanoid-robot motion generation,” *The International Journal of Robotics Research*, vol. 33, pp. 1006–1028, may 2014.
- [38] M. Marinho, L. Figueredo, and B. V. Adorno, “A dual quaternion linear-quadratic optimal controller for trajectory tracking,” in *Intelligent Robots and Systems (IROS)*, 2015 IEEE/RSJ International Conference on, pp. 4047–4052, IEEE, 2015.
- [39] T. Brox, B. Rosenhahn, J. Gall, and D. Cremers, “Combined region and motion-based 3d tracking of rigid and articulated objects,” *IEEE Transactions on Pattern Analysis and Machine Intelligence*, vol. 32, no. 3, pp. 402–415, 2010.
- [40] E. Rohmer, S. P. Singh, and M. Freese, “V-rep: A versatile and scalable robot simulation framework,” in *Intelligent Robots and Systems (IROS)*, 2013 IEEE/RSJ International Conference on, pp. 1321–1326, IEEE, 2013.
- [41] R. G. Chittawadigi and S. K. Saha, “An analytical method to detect collision between cylinders using dual number algebra,” in *Intelligent Robots and Systems (IROS)*, 2013 IEEE/RSJ International Conference on, pp. 5353–5358, IEEE, 2013.
- [42] S. Agarwal, R. A. Srivatsan, and S. Bandyopadhyay, “Analytical determination of the proximity of two right-circular cylinders in space,” *Journal of Mechanisms and Robotics*, vol. 8, no. 4, p. 041010, 2016.